THERMOELECTRIC HALF-HEUSLERS: SYNTHESIS, PROCESSING, AND PERFORMANCE

by

Joseph Robert Croteau

A thesis

submitted in partial fulfillment

of the requirements for the degree of

Master of Science in Materials Science and Engineering

Boise State University

August 2016

BOISE STATE UNIVERSITY GRADUATE COLLEGE

DEFENSE COMMITTEE AND FINAL READING APPROVALS

of the thesis submitted by

Joseph Robert Croteau

Thesis Title: Thermoelectric Half-Heuslers: Synthesis, Processing, and Performance

Date of Final Oral Examination: 30 June 2016

The following individuals read and discussed the thesis submitted by student Joseph Robert Croteau, and they evaluated his presentation and response to questions during the final oral examination. They found that the student passed the final oral examination.

Darryl Butt, Ph.D.	Chair, Supervisory Committee
Yanliang Zhang, Ph.D.	Member, Supervisory Committee
Lan Li, Ph.D.	Member, Supervisory Committee
Patrick M. Price, Ph.D.	Member, Supervisory Committee

The final reading approval of the thesis was granted by Darryl Butt, Ph.D., Chair of the Supervisory Committee. The thesis was approved for the Graduate College by Jodi Chilson, M.F.A., Coordinator of Theses and Dissertations.

ACKNOWLEDGEMENTS

It is with sincere gratitude that I acknowledge Dr. Darryl Butt for taking a chance on me, for giving me countless opportunities, and for exposing me to so many of the diversities contained within the field of materials science and engineering. I thank you for supporting both my education and the pursuit of my passions. I will be always grateful.

I acknowledge the members of my committee for their thoughtful and encouraging conversations, and for always challenging me. I also wish to thank the Boise State community and the dedicated professors who have personally influenced me, including Mike Hurley, Will Hughes, Chad Watson, and so many others. A special thanks to the staff and students of the Advanced Materials Lab, including Brian Jaques, Bryan Forsmann, Kyle Witherspoon, Allyssa Bateman, Jennifer Watkins, Kelci Lester, Jordan Vandegrift, John-Paul Stroud, and many more. For their significant contributions to this work, I thank Nick Kempf and Medha Veligatla.

This work has been funded in part by the US Department of Energy, Office of Nuclear Energy, under the award #DE-NE0008255. The purpose of which is to develop self-powered, wireless sensor networks for nuclear applications. This grant partners Boise State University with the Idaho National Laboratory, the University of Houston, and GMZ Energy.

This work has also been partially funded by the State of Idaho through the Center for Advanced Energy Studies, a consortium between Boise State University, the Idaho

National Laboratory, Idaho State University, the University of Idaho, and the University of Wyoming.

ABSTRACT

Thermoelectric half-Heusler compounds have potential to convert the heat wasted from industrial and transportation processes to useful electricity. Among the highest performing half-Heusler compounds are nano-structured bulk materials which have been arc-melted, pulverized into a nano-powder, and sintered by DC-hot press. High performing n- and p-type half-Heusler compounds with nominal composition of $Hf_{0.25}Zr_{0.75}NiSn_{0.99}Sb_{0.01}$ and $Nb_{0.75}Ti_{0.25}FeSb$, respectively, have been provided to us in both dense and powder form by our collaborators at the University of Houston. We consolidate these powders by SPS, refine these powders to improve both particle size and phase-purity, and synthesize these compositions by an alternative mechanical alloying process. In addition to these compositions, we investigate these same base compositions with different doping levels as well as compounds with different base compositions.

Through mechanically alloying processes, we are able to reduce wide distributions of grain sizes in as-received materials ranging from sub-micrometer to larger than 20 μm, to a narrow distribution of grain sizes ranging from 300 – 700 nm. Although single phase, Hf-containing half-Heusler compositions were not successfully synthesized by mechanical alloying, we demonstrate the ability to make useful quantities of single-phase, Hf-free nano-powders in a rapid, single-step process. Finally, the thermoelectric performance for several compositions of half-Heusler compounds, synthesized and consolidated by several processes, are compared.

TABLE OF CONTENTS

LIST OF TABLES

LIST OF FIGURES

CHAPTER ONE: INTRODUCTION

Motivation

From each an economic, environmental, and humanitarian perspective, society faces no greater threat than climate change.[1-3] Each year, human activity pollutes our atmosphere with unprecedented levels of heat-trapping emissions by burning coal, oil, and natural gas for energy production. For the foreseeable future world energy consumption and carbon emissions will continue to rise. Although contributions from low-carbon forms of energy, including renewables and nuclear, are projected to grow at the fastest rates of 2.6 and 2.3% per year, respectively, liquid fuels, natural gas, and coal will still account for 78% of the energy consumed in 2040.[1] This fact has, in recent years, led to increased research in renewable energy technologies, and has rejuvenated interest in thermoelectric power generation, a scientific field which largely remained stagnate for three decades, from the 1960's until the 1990's.

A testament to the reliability of thermoelectric materials is a proven history of power generation, serving 67 deep space missions extending beyond 30 years of performance.[4] A renewed interest in energy efficiency and renewable energy has encouraged many developments to traditional thermoelectric materials, such as bismuth-telluride, lead-telluride, and silicon-germanium, as well as the discovery and development of new material systems, such as skutterudites and half-Heuslers.[5] Despite these recent advancements, the thermal-to-electric conversion efficiency remains low and commercial scalability is difficult, so for the time-being, thermoelectric generators will

be limited to niche applications which are poorly served, or not served at all by existing technologies.[6,7]

Although this field faces great barriers, there is a growing focus on thermoelectric materials for energy applications, namely waste heat recovery from industrial and transportation processes.[4] Thermoelectric generators can potentially be a significant feature in the future, low-carbon energy landscape by contributing to each of the three following scenarios. Thermoelectric devices have been identified as an important nuclear enabling technology which can improve the safety and reliability of nuclear power plants by scavenging small amounts of heat at various locations to power remote, wireless sensors, even in blackout conditions.[8,9] Thermoelectric generators can increase the overall efficiency of transportation and industrial processes, which reject approximately two-thirds of consumed energy as wasted heat, by converting some of that heat directly into electricity.[4-6,10-14] Finally, thermoelectric generators can be a source of stand-alone electricity generation, or combined with other renewable energy technologies to generate power.[5,12] In order for this goal to be realized, there must be continual enhancements to thermoelectric devices across all length scales, from intrinsic material properties, to system architecture.

Thermoelectric Power Generation

A thermoelectric generator is a Carnot heat-engine. However, the "working fluid" in a thermoelectric device is electrons, and thus, a thermoelectric generator can convert thermal energy to electric energy without any moving parts, and without a gas/liquid, compression/expansion cycle.[4,6] When n- and p-type semiconducting, thermoelectric materials are electrically connected in what is known as a unicouple, and a temperature

gradient is maintained, they have the robust, solid-state capability of converting thermal energy into an electric current. When many unicouples are assembled in such a way that they are electrically in series and thermally in parallel, their overall power output is increased, and the resulting device is known as a thermoelectric generator. The method in which a thermoelectric device generates an electric current is demonstrated by a sketch of a unicouple in Figure 1. Mobile charge carriers are generated at the hot-side of a device, electrons (e^-) in the case of an n-type material and holes (h^+) in a p-type material. The increased number of charge carriers at the hot-side creates a chemical potential gradient across the device, and charge carriers will diffuse to the cold-side of the device. Equilibrium will be reached when the opposing force on the carriers resulting from the electric potential gradient established by the diffusion of charge carriers balances the chemical potential gradient. This phenomenon is known as the Seebeck effect, and the voltage generated per unit temperature is measured as the Seebeck coefficient.[15] When these materials are connected in a circuit, this established voltage will result in a useful electric current.

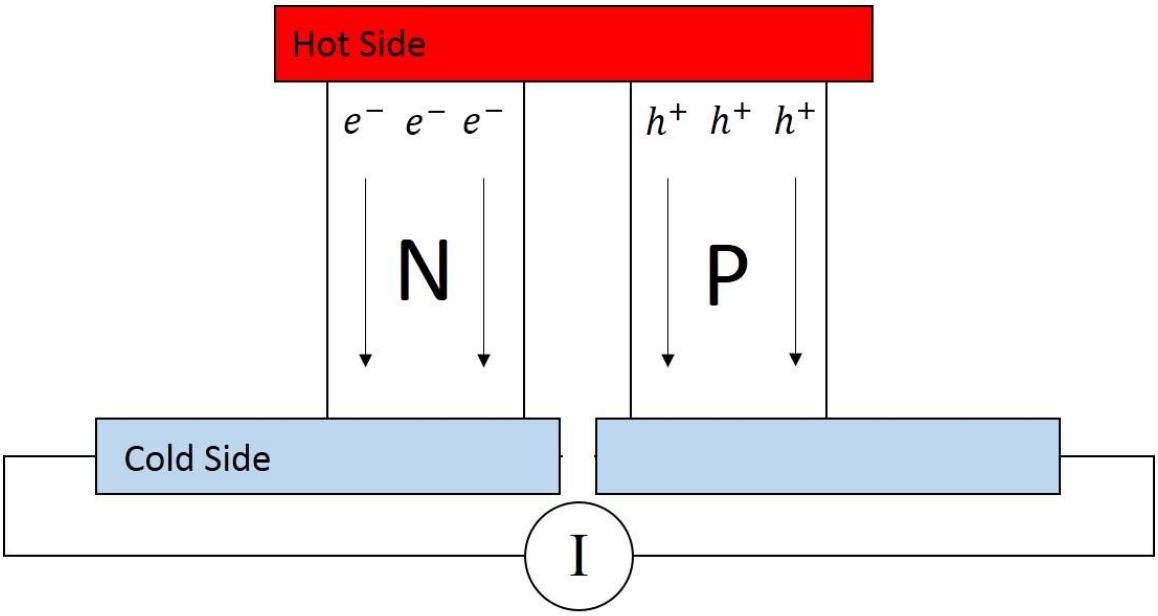

Figure 1: When n- and p-type semiconducting thermoelectric materials are connected in a circuit, and a thermal gradient is maintained, an established voltage will drive the flow of charge carriers, resulting in an electric current (I).

The performance of a thermoelectric device relies directly on three interdependent, intrinsic material properties. In addition to the Seebeck coefficient, the electric and thermal conductivities are combined to form what is known as the thermoelectric figure of merit (*ZT*), denoted:

$$ZT = \frac{S^2 \sigma}{\kappa} T$$

where *S* is the Seebeck coefficient ($V \cdot K^{-1}$), σ is the electrical conductivity ($\Omega^{-1} \cdot m^{-1}$), κ is the thermal conductivity ($W \cdot m^{-1} \cdot K^{-1}$), and *T* is the absolute temperature at which the properties are measured (*K*). *ZT* is maximized by a high Seebeck coefficient and electrical conductivity, and a low thermal conductivity, however, these three values are all influenced by the charge carrier concentration. Generally, at low carrier concentrations (i.e. $\leq 10^{21}$ cm^{-3}), the Seebeck coefficient will be high, and the thermal conductivity will be low, but so will the electrical conductivity. At high carrier

concentrations (i.e. $\geq 10^{22}$ cm^{-3}), the electrical conductivity will be high, but so will the thermal conductivity, and the Seebeck coefficient will be small. Therefore, an ideal charge carrier concentration which provides the highest peak ZT at some given temperature can be achieved with an appropriate doping level.[5]

Being that a thermoelectric generator is a heat-engine, its maximum thermal-to-electric conversion efficiency (η_{max}) can be determined by the following Carnot efficiency equation,[4] which incorporates the previously defined figure of merit (ZT).

$$\eta_{max} = \frac{T_{hot} - T_{cold}}{T_{hot}} \quad \frac{\sqrt{1 + ZT} - 1}{\sqrt{1 + ZT} + \frac{T_{cold}}{T_{hot}}}$$

Like any heat-engine, the efficiency of a thermoelectric generator is maximized by the largest difference in temperature across the hot side (T_{hot}) and the cold side (T_{cold}) of the device. Although having a high peak ZT is important, a good thermoelectric material should have a high effective average ZT across the temperature range from T_{hot} to T_{cold}. Although many state-of-the-art thermoelectric materials have a peak ZT $\approx$ 1, their effective average ZT ranges from about 0.55 to 0.75, meaning that current thermoelectric materials convert only 10 to 15% of the available Carnot efficiency. When considering electric and thermal losses in a device, the overall efficiency of state-of-the-art thermoelectric generators is about 3 to 6.5%.[4] For a thermoelectric generator to be competitive with combustion engines and other power converting technologies, peak ZT values must reach well over 2,[10,13,15] which will require significant enhancements to existing thermoelectric materials, as well as developing new ones.

The first strategy to maximize a material's ZT is to select an appropriate doping level which balances a high Seebeck coefficient and electrical conductivity to maximize

the so-called power factor ($S^2\sigma$). Secondly, a low thermal conductivity is crucial for maximizing ZT and maintaining as large a temperature gradient as possible across the thermoelectric device. A material's thermal conductivity is determined by both an electronic component and a lattice component. In other words, heat is carried in a material by electronic charge carriers and by phonons, or lattice vibrations, so that the total thermal conductivity is expressed as:

$$\kappa_{Total} = \kappa_{electronic} + \kappa_{lattice}$$

Where the electronic component is defined by the Wiedemann-Franz relationship:

$$\kappa_{electronic} = L\,\sigma\,T$$

with σ being the electrical conductivity and *T* being temperature. *L* is the Lorenz number, defined as:

$$L = \frac{\pi^2}{3}\left(\frac{k_b}{e}\right)^2$$

where k_b is the Boltzmann constant and *e* is the elementary charge. The Lorenz number is generally assumed to retain a constant value in most metals of $2.44 \cdot 10^{-8}$ ($W\,\Omega\,K^{-2}$) across all temperatures, however it has shown to have a very slight dependence on temperature.[16]

Recent multi-scale strategies, known collectively as phonon engineering, have been developed to decouple these two mechanisms of heat transfer.[5,15,17,18] More specifically, these strategies aim to suppress the heat conducted by phonons without negatively affecting electronic charge carriers. One can take advantage of the fact that the mean free path of an electron is about 1-100 nm, whereas that of a phonon is about 1-500 nm. By introducing structural features on this length-scale, one can effectively filter out heat-carrying phonons without greatly effecting the path of an electron. These

features can take the form of atomic-scale defects, such as interstitial or substitutional atoms, nano-scale precipitates or inclusions, as well as grain boundaries (Figure 2). In fact, these strategies have been shown to increase the ZT of a nano-structured material by up to 60% compared to its bulk-counterpart.[19] Furthermore, electrically-active precipitates (i.e. semiconducting or metallic inclusions) have not only been effective at suppressing phonon transport, but can add or subtract charge carriers to enhance electrical properties.[10] Of these strategies, perhaps the simplest are to create a solid-solution (alloy) or to increase the number of grain boundaries by reducing the average grain size into the 100-500 nm range. What is known as alloy scattering is accomplished by the isoelectronic substitution of a host atom with a foreign atom, and local strain fields and mass fluctuations introduce phonon scattering centers.[16] In other words, intentionally replacing a solvent atom with a solute atom of the same valence but with a different atomic size, for example titanium, zirconium, and hafnium, results in random crystal variations which strongly influence the behavior of phonons. However, this is not without consequences, and enhancements to thermal conductivities are offset by diminishes to carrier mobility.[16] Although lower carrier mobility benefits Seebeck coefficient, it has a greater, negative effect on electrical conductivity. Much like doping, there is an appropriate level of alloying which will balance the negative effects of electrical conductivity with the enhancements to the Seebeck coefficient and to the thermal conductivity.

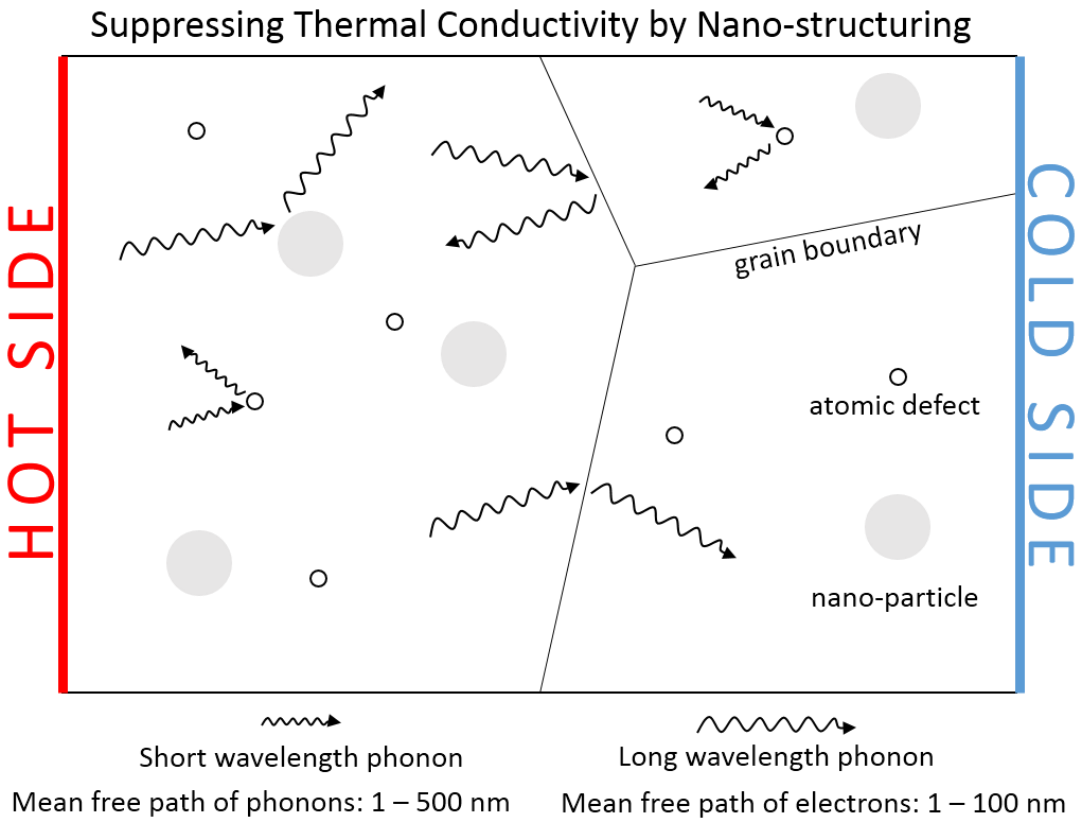

Figure 2: Examples of how phonons traveling from the hot to cold side in a material can be scattered by atomic defects, nano-particles, and grain boundaries. The result of which is a suppression of the lattice component of thermal conductivity.

Thermoelectric Half-Heuslers

More than 1500 different ternary compositions of intermetallic compounds comprise the class of Heusler compounds with 2:1:1 stoichiometry.[20] A sub-class of Heusler compounds with 1:1:1 stoichiometry are known as half-Heusler compounds. Both of these structures, illustrated in Figure 3, can be described as having four-interpenetrating, face-centered cubic lattices. In the X_2YZ Heusler structure, all lattice sites are occupied by metallic elements, whereas in the XYZ half-Heusler structure (space group no. 216, $F\bar{4}3m$) only three of the four lattice sites are occupied by metallic elements, with the fourth lattice remaining vacant. The occupied sites in the half-Heusler structure correspond to the Wyckoff positions 4a (0, 0, 0), 4b (½, ½, ½), and 4c (¼, ¼,

¼).[20] In these compounds, the X site (4a) is typically occupied by an early transition metal (group 3 – 6), an alkali metal (group 1 – 2), or a rare earth metal of the lanthanide series, the Z site (4b) is typically occupied by a main group element (group 13 – 16), and the Y site (4c) is typically occupied by a transition metal from group 7 – 12..[20]

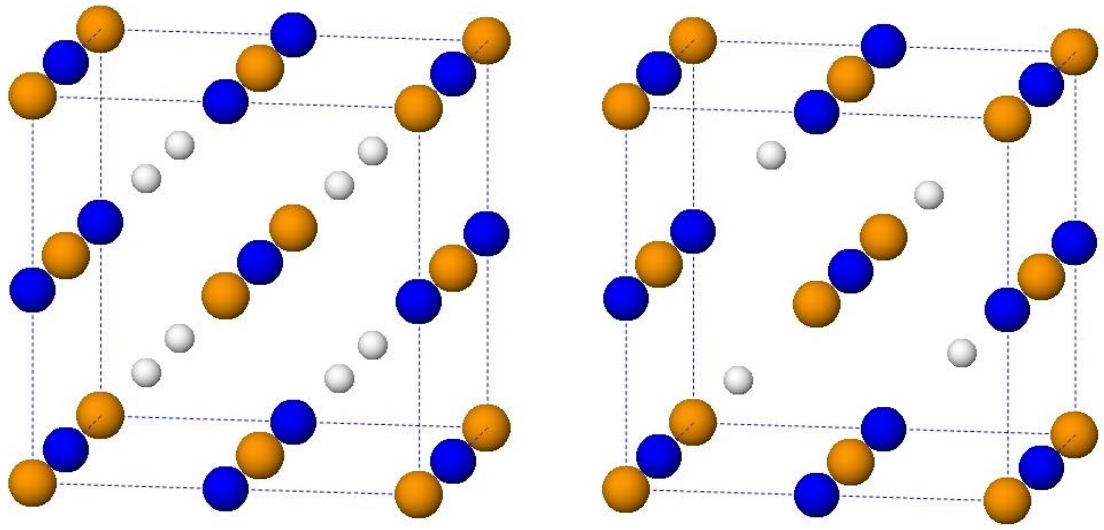

Figure 3: The fully occupied X_2YZ Heusler structure (left) compared to the XYZ half-Heusler structure (right). Elements with a large difference in electronegativity occupy the X and Z sites, represented respectively by orange and blue spheres, form an anionic framework. The Y site, represented by a white sphere, is typically occupied by a transition metal.

The structure of half-Heusler compounds is successfully described using the principles of Zintl chemistry.[21] In these compounds, elements with a large difference in electronegativity exchange valence electrons to form an anionic framework and a closed valence shell configuration. Consider, for example, the ternary half-Heusler compound ZrNiSn, which has a total of 18 valence electrons per XYZ formula unit: zirconium and tin which each contribute four valence electrons, and nickel which contributes ten. Zirconium donates all four of its d-orbital electrons to the more electronegative element, tin, to fill its p-orbital, and these two elements form a cubic framework. Nickel, with 10

localized valence electrons filling its non-bonding d-orbital, sits loosely bound in the tetrahedral-coordinated, interstitial sites. Interactions between nickel and zirconium result in a splitting of their d-orbitals, which gives rise to an observable band gap in the ZrNiSn half-Heusler compound. This concept provides a simple counting rule which says that any ternary half-Heusler compound with 18 valence electrons per formula unit should possess a band gap, therefor making it a semi-conductor, and a suitable candidate for thermoelectric applications. Furthermore, once a ternary composition with 18 valence electrons is selected, the fact that so many elements can crystallize in a half-Heusler structure means there are many possibilities to substitute atoms at each the X, Y, or Z sites to optimize transport properties. For example, in the ZrNiSn compound, zirconium can be partially substituted with titanium and hafnium (equal valence) to enhance alloy scattering, and tin can be partially substituted with antimony (greater valence) to tune the charge carrier concentration.

Building off of the simple rule that a half-Heusler should have 18 valence electrons to be a semiconductor, there have been several recent attempts which make use of first principle calculations to predict new compositions of half-Heusler compounds suitable for power generation.[22,23] These approaches first calculate a band gap, and then predict an optimum doping level to maximize power factor. It should be noted that several compositions of half-Heusler compounds, such as ZrNiSn and TiCoSb, were known to have good thermoelectric properties before studies like these were conducted, but it was not until after studies like these before some new compositions were investigated, such as NbFeSb.

Since the late 1990's, there has been growing interest in half-Heusler compounds for thermoelectric applications, and there is currently a broad base of enthusiasm to support using these materials for waste heat recovery and power generation in the temperature range of about 450°C to 750°C.[5,10,11,19] These materials are typified by high a Seebeck coefficient and electrical conductivity, meaning that they are capable of achieving very high power factors. Of these compounds, by far the most studied have been of the (M)NiSn and the (M)CoSb type materials, where (M = Hf, Zr, Ti).[10,11,19,21,24] When compared to other thermoelectric materials suitable for this temperature range, such as lead-chalcogenides and skutterudites, half-Heusler compounds are more attractive because they do not rely on toxic elements like lead or low-abundant elements such as ytterbium.[11] Comprised of low-toxicity and earth-abundant metals, half-Heusler compounds also have higher strength then chalcogenides, and greater thermal stability than skutterudites.[11] However, half-Heusler materials suffer from very high thermal conductivities, often much greater than about 7 $W \cdot m^{-1} \cdot K^{-1}$, which keep them from realizing a high ZT. Recently, by incorporating phonon engineering strategies, such as alloy scattering and nano-structuring, there has been significant progress in reducing thermal conductivity in these materials below about 4 $W \cdot m^{-1} \cdot K^{-1}$.[5,10,19]. Now, thermoelectric figures of merit of $ZT \approx 1$ are routine in n-type (M)$NiSn_{1-x}Sb_x$ and p-type (M)$CoSb_{1-x}Sn_x$ half-Heusler compounds where M = (a combination of Hf, Zr, and Ti).[5,10,11,15,16,19,24-44] Theoretically, half-Heusler compounds could reach a thermal conductivity as low as 1 $W \cdot m^{-1} \cdot K^{-1}$,[10] which could provide a route for achieving a figure of merit of $ZT \gg 2$.

Not only is high thermoelectric performance sought in half-Heusler compounds, but there are ongoing efforts to drive down the raw material and synthesis costs of these materials. One avenue is to achieve low thermal conductivities in high-performing compositions while reducing or eliminating the reliance on hafnium, which is about eight-times the cost of zirconium, and sixty-times the cost of titanium. Another avenue is to reduce the overall energy required to synthesize large quantities of half-Heusler materials. Currently, the most popular methods of producing useful quantities of fine half-Heusler powders have been to cast an ingot using either arc- or induction-melting, followed by pulverizing the ingot in a mill to produce a powder.[11] However, these methods are notoriously difficult for alloying elements with a large difference in melting temperature, such as Hf ($T_m \approx 2200$ °C) and Sn ($T_m \approx 230$ °C), because the element with a lower melting temperature may vaporized during the process. It is therefore difficult to control the composition of an intermetallic compound prepared in this manner. What's more, the low melting temperature element in half-Heusler compounds is typically the intended dopant (i.e. Sn and Sb), making it difficult to control the electronic charge carrier concentration. In order to combat this evaporative loss, many authors report adding arbitrarily excess amounts of tin or antimony.[11]

While there are other methods to produce homogenous half-Heusler materials, including lengthy solid state reactions, optical floating zone melting, and microwave heating, these techniques each have their limitations.[11] An alternative, and largely unexploited technique to prepare half-Heusler powders is mechanical alloying. Although these techniques have been used successfully to produce other thermoelectric materials such as various bismuth telluride and silicon germanium compositions, mechanical

alloying has shown only moderate success when applied to half-Heuslers.[11,35,36,45,46] In these previous attempts, if a half-Heusler phase was synthesized, it was often accompanied by very large quantities of other intermetallic compounds. It is a common misbelief that ball milling does not produce sufficient energies to successfully alloy high-melting temperature elements such as Hf and Zr, and for that reason it has been generally avoided as a method to synthesize half-Heusler compounds.[11] However, if mechanical alloying can be demonstrated as a successful technique for producing useful quantities of single-phase, half-Heusler nano-powders, it could become a preferred synthesis method. The advantage of this technique is that it eliminates several previously-required high temperature processes which resulted in evaporative loss of low melting point elements, and are likely sources of contamination from both oxidation and copper impurities introduced by arc-melting hearths. Furthermore, mechanical alloying has great upscaling potential to produce batches ranging from tens to hundreds of kilograms.[47]

Common methods to rapidly sinter these fine-powders into a useful dense part include DC-assisted hot pressing, spark plasma sintering (SPS), and shock consolidation.[11] It is important to limit both the time and temperature to as low as possible to preserve nanoscale features and to limit the amount of evaporative loss of high vapor pressure elements such as Sn and Sb. For these reasons, the rapid DC-hot press and SPS processes have become the prevailing method presented in literature to consolidate laboratory-scale quantities of materials. However, because of its importance to commercial-scale manufacturing, especially with regards to tape-casting, screen printing, and 3D printing, conventional sintering techniques should not be disregarded.

In addition to thermoelectric performance, low-cost, and availability of raw materials being important factors for commercialability, one must also consider the compatibility of n- and p-type materials. The two compositions ought to have comparable thermal stability and coefficients of thermal expansion (CTE). However, with regards to half-Heusler compounds, historically well-performing n- and p-type materials have had very different compositions, resulting in a large mismatch in CTE.[21] The result of this mismatch will be large thermal stresses developing while operating a device, reducing its longevity and reliability. There is, for this reason, a desire to develop high performing, n- and p-type half-Heusler compounds with the same base composition, thus having the same, or nearly the same, CTE. In fact, the transition from n-type to p-type conduction has been demonstrated once before in a TiNiSn based half-Heusler compound. In that work, Ouardi *et al*.[48] shows that lowering the net valence electron count below 18 per formula unit by partially substituting Ti with the lower valence Sc resulted in holes being the majority carrier. In turn, by partially substituting Ti with the higher valence V, electrons were the majority carrier. Not only does this highlight the flexibility of half-Heusler compounds to incorporate substitutions on each the X, Y, and Z sites, but provides a promising route to achieve both n- and p-type conduction in the same material, all but eliminating concerns of mismatching coefficients of thermal expansion.

In the current work, three different base compositions of half-Heusler compounds, including ZrNiSn, NbFeSb, and NbCoSn, are investigated. The compound with nominal composition of $Hf_{0.25}Zr_{0.75}NiSn_{0.99}Sb_{0.01}$ is the highest achieving n-type half-Heusler compound with the lowest concentration of Hf.[11] In this material, isoelectronic substitution of Hf for Zr greatly reduces lattice thermal conductivity, and doping Sb for

Sn optimizes electrical properties, providing a ZT ≈ 1 at 700 °C. The compound with nominal composition of $Nb_{0.75}Ti_{0.25}FeSb$ is among a very recently developed group of high performing, p-type half-Heusler materials.[44,49] In this material, substituting a relatively large amount of Ti for Nb introduces holes to maximize its electrical properties, as well as lowering thermal conductivity via alloy scattering. These two materials were provided as both nano-powders and as dense pellets by Dr. Zhifeng Ren's research group at the University of Houston. Additionally, the half-Heusler compound with base composition NbCoSn, which has received very little attention in published literature, is investigated as a Hf-free alternative to the n-type ZrNiSn materials. Furthermore, attempts are made to dope this composition with holes to make a new p-type material. All three of these materials are synthesized by a mechanical alloying technique in hopes to provide an alternative manufacturing route. Spark plasma sintering is used to rapidly consolidate these powders to retain nano-scale features in a bulk part and to reduce the amount of time spent at high temperatures to limit evaporative loss. The Seebeck coefficient, electrical conductivity, and thermal conductivity are all measured and used to calculate a ZT for each material. Finally, a discussion of microstructural features and chemical composition supports the various behaviors in thermoelectric performance of each material.

CHAPTER TWO: MATERIALS AND METHODS

ZrNiSn Based Half-Heusler Compounds

Benchmark ZrNiSn based half-Heusler compound with a nominal composition of $Hf_{0.25}Zr_{0.75}NiSn_{0.99}Sb_{0.01}$ was provided in both dense and powder form by our collaborators in Dr. Zhifeng Ren's research group at the University of Houston. This material is among the highest performing n-type half-Heusler compounds.[11] This material realizes a low thermal conductivity, even with a low Hf-concentration, by phonon scattering because of its so-called nano-structuring, or sub-micrometer grains.[29] First, a homogenous ingot is arc-cast from high-purity, raw metals in powder form. Appropriate amounts of each elemental powder are weighed to achieve the desired stoichiometry, including an arbitrarily-excess amount of 5% extra Sn and Sb to compensate for evaporative loss, and then placed in the water-cooled copper-hearth of an arc-melting furnace (Model 5TA Reed Tri-Arc Furnace, CENTORR Vacuum Industries, USA). Powders are then melted in the three-electrode, inert-atmosphere arc-melter, cooled, flipped, and then re-melted several times to ensure homogenous melting and mixing. The cast ingot is then crushed into a fine powder using a high-energy ball mill for between 4 and 20 hours (8000M Mixer/Mill, SPEX SamplePrep, USA). More details can be found elsewhere in published literature.[30] Powders synthesized in this manner will be referred to herein as the as-received material.

These same powders were consolidated by our collaborators using a custom DC-hot press, and provided to us in dense form. This custom DC-hot press was built in-house using a large DC power supply and a modified hydraulic pellet press (Carver, Inc., USA). In this method, powders are loaded into graphite-lined, graphite dies (typically ½" or 1" diameter), compressed between the platens of the hydraulic press (which also serve as electrodes), and a constant DC current is passed through the sample and die which results in resistive-heating. While operating in lab-air, the sample and die is heated to 1000 °C and held for two minutes. Samples prepared by this method have greater than 95% density when measured by the Archimedes method. From herein, materials received in dense form consolidated by the DC-hot press will be referred to as the benchmark material.

The as-received powders were refined in order to reduce the particle size and to narrow the particle size distribution. In approximately 10 gm batches, as-received powder was loaded into a 250 ml hardened-steel milling vessel with 100 gm of 5 mm, 440C stainless steel milling media, and sealed in an argon glovebox (<1.0 ppm O_2, <0.1 ppm H_2O). The as-received powder was then milled in a high-energy planetary ball mill (PM 100, RETSCH, Germany) for 12 hours at 500 rpm. To summarize, the refined powder was first arc-melted to produce a single-phase ingot, that ingot was crushed into a powder using a SPEX ball mill, and then milled for an additional 12 hours in a high-energy planetary ball mill. From herein, this powder will be referred to as the refined material.

In addition to the as-received powder, material with the same, or similar, nominal compositions were directly synthesized by a mechanical alloying technique. In this

approach, appropriate amounts of elemental powder to achieve the desired stoichiometry were weighed, and then placed in a 250 ml hardened steel milling vessel (All powders: Alfa Aesar, 99.5% pure or greater, 60 mesh or finer). The quantities of each elemental powder needed to produce a 10 gm batch of half-Heusler powder are given in Table 1. Because this is a room temperature synthesis method, no amount of excess material was added to compensate for evaporative loss. The vessel was "charged" with a 10:1 mass ratio of 5 mm, 440C stainless steel milling media to powder. The milling vessel was sealed in an argon glovebox. Mechanical alloying was carried out in a high-energy planetary ball mill at 350 or 500 rpm for between 12 and 100 hours. These powders will be referred to herein as mechanically alloyed or mechanically synthesized materials.

Table 1: Masses of elemental powder required to achieve the nominal half-Heusler composition in 10 grams of ZrNiSn based, mechanically synthesized nano-powders.

Nominal Composition	Mass of Elemental Powder (grams)					
	Hf	Zr	Ti	Ni	Sn	Sb
$Hf_{0.5}Zr_{0.25}Ti_{0.25}NiSn_{0.99}Sb_{0.01}$	2.9605	0.3970	0.7565	1.9470	3.8986	0.0404
$Hf_{0.5}Zr_{0.5}NiSn_{0.99}Sb_{0.01}$	3.0710	0.8236	- - -	2.0196	4.0440	0.0419
$Hf_{0.25}Zr_{0.75}NiSn_{0.99}Sb_{0.01}$	2.3043	3.5331	- - -	3.0309	6.0688	0.0629

NbFeSb Based Half-Heusler Compounds

Benchmark NbFeSb based half-Heusler compound with a nominal composition of $Nb_{0.75}Ti_{0.25}FeSb$ was provided in both dense and powder form by our collaborators in Dr. Zhifeng Ren's research group at the University of Houston. This material is a very recently developed p-type half-Heusler compound which shows promise for power harvesting applications due to its high power factor.[44] In this case, substitution of Ti for Nb serves both as a charge carrier donor, as well as to lower thermal conductivity by

alloying. Fine grained powders were synthesized in an identical manner as described previously for n-type ZrNiSn based compounds. In other words, p-type, NbFeSb materials were first arc-melted and then crushed to produce the desired nano-powder. Again, an arbitrarily excess amount of 5% extra Sb was added to compensate for evaporative loss during the arc-melting process. These powders were also consolidated by the custom DC-hot press at 1000 °C for two minutes. Herein, materials received in dense form will be referred to as the benchmark material, and those received in powder form will be referred to as the as-received material.

The as-received, p-type material with nominal composition $Nb_{0.75}Ti_{0.25}FeSb$ was also refined by an additional ball milling step, as described previously, at 500 rpm for 12 hours. These powders will be referred to as the refined material. In addition to as-received materials, powders of the same, or similar, composition were directly synthesized through a mechanical alloying approach. These will be referred to as the mechanically alloyed or mechanically synthesized materials. The quantities of each elemental powder needed to produce a 15 gm batch of half-Heusler powder is given in Table 2.

Using first-principle calculations, Yang *et al.*[23] predicted the maximum room-temperature power factor could be achieved by an optimum doping level of -0.045 electrons per unit cell in a NbFeSb compound. Furthermore, Joshi *et al.*[44] used first-principle calculations to show the Seebeck coefficient reaches nearly 200 $\mu V \cdot K^{-1}$ and resistivity exceeds 15 $\mu\Omega \cdot m$ at 800°C in a NbFeSb doped with -0.05 electrons per unit cell. The current study attempts to confirm these predictions by mechanically synthesizing and spark plasma sintering a material with nominal composition

$Nb_{0.96}Ti_{0.04}FeSb$, assuming each Ti atoms donates one hole. Recently, Fu *et al.*[49] reported a record-high ZT ≈ 1.5 for a p-type half-Heusler with a nominal composition of $Nb_{0.88}Hf_{0.12}FeSb$. The current study aims to duplicate those findings in a mechanically synthesized material.

Table 2: Masses of elemental powder required to achieve the nominal half-Heusler composition in 15 grams of NbFeSb based, mechanically synthesized nano-powders.

Nominal Composition	Mass of Elemental Powder (grams)				
	Nb	Ti	Hf	Fe	Sb
$Nb_{0.75}Ti_{0.25}FeSb$	4.0316	0.6924	- - -	3.2311	7.0449
$Nb_{0.96}Ti_{0.04}FeSb$	4.9788	0.1069	- - -	3.1174	6.7969
$Nb_{0.88}Hf_{0.12}FeSb$	4.3677	- - -	1.1443	2.9834	6.5047

NbCoSn Based Half-Heusler Compounds

Although the (M)NiSn and (M)CoSb type compounds have received the most attention, there are dozens of other half-Heusler compounds which could have good thermoelectric properties.[50] Using a first principles approach, Yang *et al.*[23] evaluated the thermoelectric properties of more than thirty half-Heusler compounds. Of those investigated, compounds with the base composition NbCoSn stand out, having a maximum power factor nearly twice as high as the power factor calculated for the (M)NiSn compounds when doped n-type, and about equal to that of the (M)CoSb compounds when doped p-type. This makes the NbCoSn based half-Heusler compound a potential alternative to existing n-type materials, and a candidate for n- and p-type doping. Despite having such promising theoretical values, very little experimental attention has been paid to the NbCoSn type compounds. To the best of the author's

knowledge, this compound has never been tested in the p-type regime, and only twice in the n-type regime.

In 2006, Ono *et al.*[51] reported a promising ZT of 0.3 in a $NbCoSn_{0.9}Sb_{0.1}$ compound prepared from arc-melted and crushed powders. Although this material had good electrical properties, it was plagued by impurities, low density, and large grains up to 90 μm. In 2008, Kimura *et al.*[52] confirmed this ZT of 0.3 in a directionally solidified $NbCo_{1.05}Sn$ compound prepared by the optical floating zone melting method. An important difference is that Ono *et al.* tuned the carrier concentration by substituting Sb for Sn, while Kimura *et al.* achieved the same ZT in a dense, nearly-single phase material without any attempt to optimize the carrier concentration. Kimura *et al.* went on to show that the presence of Nb_3Sn, Co_7Nb_6, and $NbCo_2Sn$ intermetallic phases in slightly-off stoichiometric compounds contributed to metal-like behavior (i.e. lower Seebeck coefficient and higher electrical conductivity).

In the current study, NbCoSn based half-Heusler compounds are prepared through the direct mechanical synthesis route previously described. Half-Heusler powders were mechanically synthesized directly from the powder form of the constituting elements. Four different NbCoSn based compositions were synthesized in 15 gm batches by adding the appropriate mass of each element given in

Table 3. These powders were sealed in a 250 ml hardened-steel milling vessel with a 10:1 mass ratio of 5 mm, 440C stainless steel media to powder, and milled in a high-energy planetary ball mill. They were milled initially for 4 hours at 350 rpm, followed by 6 to 24 hours at 500 or 600 rpm, and finally another hour at 350 rpm.

Table 3: Masses of elemental powder required to achieve the nominal half-Heusler composition in 15 grams of NbCoSn based, mechanically synthesized nano-powders.

Nominal Composition	Mass of Elemental Powder (grams)				
	Nb	Ti	Co	Sn	Sb
$NbCoSn_{0.9}Sb_{0.1}$	5.1452	- - -	3.2637	5.9168	0.6743
$Nb_{0.9}Ti_{0.1}CoSn$	4.7144	0.2699	3.3227	6.6930	- - -
$Nb_{0.75}Ti_{0.25}CoSn$	4.0310	0.6923	3.4093	6.8674	- - -
$Nb_{0.25}Ti_{0.75}CoSn$	1.4715	2.2744	3.7336	7.5206	- - -

Spark Plasma Sintering

Each of the as-received, refined, and mechanically synthesized materials of ZrNiSn and NbFeSb base compositions were consolidated under various conditions ranging from 925 to 1050 °C by spark plasma sintering (SPS-515S, Dr. Sinter, Japan). In a nitrogen glovebox, powders were loaded into 12.5 mm graphite-lined graphite dies, pre-compacted under 30 MPa of applied pressure, and then sintered in a vacuum atmosphere of less than 75 mTorr with 100 MPa of pressure applied throughout sintering. Temperature, measured by a K-Type thermocouple inserted into a hole bored half-way through the wall of the die, was ramped at 150 °C/min to 50 °C below the maximum sintering temperature, and then ramped at 50 °C/min to the maximum sintering temperature. It was then held at that temperature for 5 or 10 minutes according to the matrix in Table 4. After dwelling at the maximum sintering temperature, the die and sample were allowed to cool naturally to ambient, at which time the pressure was relieved and the sample was introduced to lab-air. Pellets sintered under any condition were all > 99% theoretical density measured by Archimedes' method.

Table 4: Spark plasma sintering conditions for as-received, refined, and mechanically synthesized half-Heusler compounds with ZrNiSn, NbFeSb and NbCoSn base compositions. In all cases, powders were sintered in a 12.5 mm graphite die in a vacuum atmosphere of less than 75 mTorr with 100 MPa of pressure applied throughout sintering. Temperature, measured by a K-Type thermocouple inserted into a hole bored half-way through the wall of the die, was ramped at 150 °C/min to 50 °C below the maximum sintering temperature, and then ramped at 50 °C/min to the maximum sintering temperature.

Nominal Composition	Spark Plasma Sintering Conditions	
	Sintering Temperature (°C)	Dwell Time (min)
$Hf_{0.25}Zr_{0.75}NiSn_{0.99}Sb_{0.01}$	1050	5
	1050	10
	975	10
$Nb_{0.75}Ti_{0.25}FeSb$	975	10
	925	10
	925	5
$Nb_{0.96}Ti_{0.04}FeSb$	975	10
All NbCoSn compositions	975	10

These pellets were prepared for microscopy by grinding through a series of water-lubricated SiC discs from 240 to 1200 grit, followed by a final polish with water based polycrystalline diamond suspensions with 1 and 1/3 μm particles on cloth pads. Between each step, samples were washed with soap and water, rinsed with DI water and isopropyl alcohol, and then blown dry with compressed air. The grain structure could be revealed by immersing the sample in Marble's reagent (50 ml DI water: 50 ml HCl: 10 gm $CuSO_4$) for 10 seconds. Samples were then immediately rinsed with DI water to terminate the etching process, sonicated in isopropyl alcohol, and blown dry with compressed air.

Thermoelectric Measurements

The performance of a thermoelectric device relies directly on the intrinsic material property known as its thermoelectric figure of merit (*ZT*), denoted:

$$ZT = \frac{S^2 \sigma}{\kappa} T$$

where *S* is the Seebeck coefficient ($V \cdot K^{-1}$), σ is the electrical conductivity ($\Omega^{-1} \cdot m^{-1}$), κ is the thermal conductivity ($W \cdot m^{-1} \cdot K^{-1}$), and *T* is the absolute temperature at which the properties are measured (*K*). In order to measure these properties, the parallel faces of 12.5 mm disks were ground to a thickness of about 1.5 mm, and polished with 1200 grit SiC polishing paper. These disks were coated with an aerosol spray graphite powder to provide an intimate contact with a good black-body absorber, and their temperature dependent thermal diffusivity was measured with a laser flash apparatus (Linseis LFA 1000, Germany); the thermal conductivity was determined based on this value, the measured density, and the specific heat of the compound calculated by the Kopp-Neumann law using published values of specific heat in either the JANAF or Barin tables. The Kopp-Neumann law states that the specific heat of a compound or alloy is equal to the molar-average of its constituents. In order to validate this law, the calculated specific heats of the half-Heusler compounds in the current study were compared to published values of specific heat, if available, obtained by differential scanning calorimetry (DSC).[29,44] The calculated values were consistent with measured values, falling within the reported margin of error for DSC measurements.

After removing the residual graphite layer with 1200 grit SiC polishing paper, rectangular bars were then cut from these disks with an oil-lubricated slow speed saw, measuring approximately 1.5 x 1.5 x 12 mm. The Seebeck coefficient and electrical

resistivity from room temperature to 600 °C was measured simultaneously in a helium atmosphere with a commercial device (Linseis LSR-3 Seebeck, Germany).

CHAPTER THREE: RESULTS AND DISCUSSION

Materials Characterization: ZrNiSn Based Compounds

Benchmark, n-type half-Heulser compound with nominal composition $Hf_{0.25}Zr_{0.75}NiSn_{0.99}Sb_{0.01}$ prepared through an arc-melting and crushing process and consolidated by DC-hot press was provided in dense form by our collaborators. These materials are characterized by about 5% porosity and grains ranging from less than 1 μm to larger than 20 μm (Figure 4). Energy dispersive X-ray spectroscopy (EDS) identified regions of pure hafnium in the sintered pellets, believed to be unmixed by the arc-melting process. Electron backscatter diffraction (EBSD) analysis confirms that large grains in the sintered pellets are a single crystal and not an agglomeration of smaller crystallites (Figure 5). This same compound was provided in powder form and consolidated by the SPS process described previously. Backscattered electron micrographs compare the as-received powder sintered by SPS to the benchmark material in Figure 6, highlighting the similarity in grain size distribution and the difference in porosity, with the benchmark material being about 5% porous and the as-received powder sintered by SPS being less than 1% porous. Contrast from grain-to-grain in these images is believed to result from slight compositional variations in each grain. A series of EDS point scans were performed on “black” grains, “grey” grains, and “white” grains, or those with the least contrast, intermediate contrast, and the most contrast. The average concentration, and the

standard deviation from 10 individual point scans from 5 separate grains of each shade, are presented in Table 5.

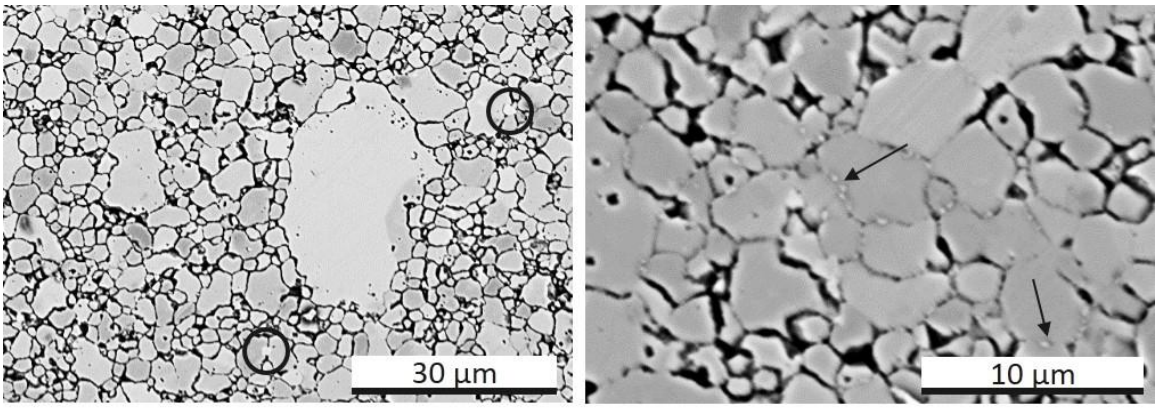

Figure 4: Backscattered scanning electron micrographs of the benchmark n-type half-Heulser compound with nominal composition $Hf_{0.25}Zr_{0.75}NiSn_{0.99}Sb_{0.01}$. These images clearly illustrate grains ranging from sub-micrometer to larger than 20 µm. Regions of unmixed Hf, identified by EDS, are circled in the left image, and indicated by arrows at grain boundaries in the right image.

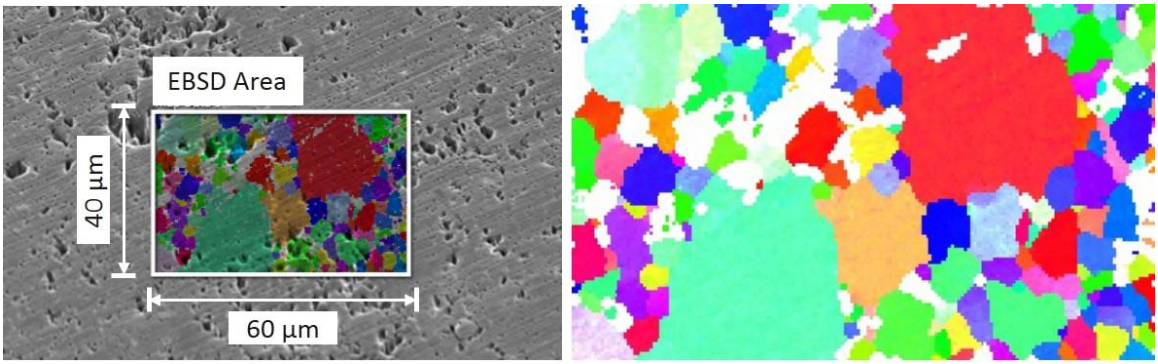

Figure 5: The surface of the benchmark, n-type half-Heusler compound on which EBSD analysis was performed. The EBSD scan area in the left image is enlarged in the right image. Each color indicates a unique crystallographic orientation, highlighting grains ranging from sub-micrometer to larger than 20 µm.

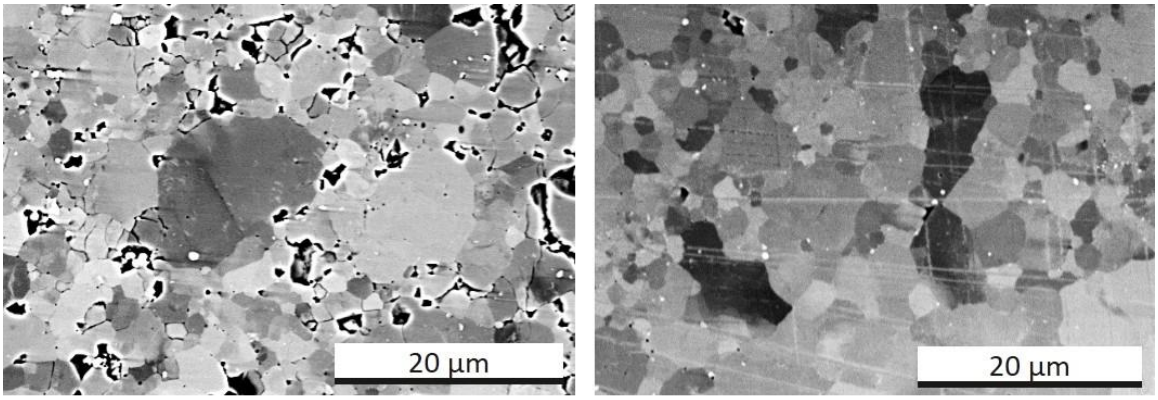

Figure 6: Backscattered SEM of (left) benchmark, n-type half-Heusler compound with nominal composition of $Hf_{0.25}Zr_{0.75}NiSn_{0.99}Sb_{0.01}$ compared to (right) the as-received material of the same composition sintered by SPS. Grain size distribution is similar in both materials, however, the benchmark material is more porous.

Table 5: The average composition determined by EDS point scans of grains with varying contrast in as-received, n-type, half-Heulser compounds with a nominal composition of $Hf_{0.25}Zr_{0.75}NiSn_{0.99}Sb_{0.01}$ sintered by SPS. Refer to Figure 6 for an example of grain-to-grain contrast.

Contrast level	Composition determined by EDS point scans				
	Hf	Zr	Ni	Sn	Sb
Black	0.27 ± 0.010	0.69 ± 0.012	1.03 ± 0.007	0.98 ± 0.005	0.02 ± 0.002
Grey	0.26 ± 0.003	0.72 ± 0.008	1.02 ± 0.009	0.98 ± 0.004	0.02 ± 0.003
White	0.26 ± 0.004	0.71 ± 0.008	1.02 ± 0.016	0.98 ± 0.006	0.03 ± 0.007

This EDS analysis suggests that there is compositional variation from grain-to-grain, namely in the Hf : Zr ratio. The grains with the least contrast have an apparently higher concentration of Hf than their surrounding grains, as well as a higher concentration than what was intended in the nominal composition. This finding is perhaps counterintuitive because one should expect that a higher concentration of Hf, which has the largest atomic mass of any element here, would produce the most contrast in an SEM image. This elemental analysis also suggests a consistent 2 – 3 % excess

amount of Ni and a 2 % substitution of Sb for Sn rather than the intended 1 %. A deviation from the intended concentration by the actual concentration of Sn and Sb is, ultimately, not surprising because of the difficult-to-control arc-melting process used to make these materials, and the excess amount of Sn and Sb added to combat evaporative loss. The excess Ni content and grain-to-grain variability is commensurate with published literature, and there is growing support for the notion that the electrical transport properties of (M)NiSn based compounds can *only* be explained by the in-gap states arising from interstitial Ni atoms occupying the nominally vacant 4d site in the half-Heusler structure.[21] Three to four distinct half-Heusler phases of $M_{1-x}M'_xNi_{1+y}Sn$ compositions have been reported in (M)NiSn based half-Heusler compounds when (M = Hf, Zr),[53] which agrees with the present work and explains compositional variation amongst grains. Furthermore, rather than being statistically distributed throughout the host phase, Ni interstitials, up to 8 at. %, have been shown to manifest as segregated full-Heusler phases ranging in scale from a few unit cells to macroscopically visible inclusions.[54] This is especially true for half-Heusler compounds prepared by induction- or arc-melting because the full-Heusler, $(M)Ni_2Sn$ phase crystallizes first from the melt, and then reacts with the remaining (M) – Sn binary phases and elemental Sn to form the intended half-Heusler phase.

Materials Characterization: NbFeSb Based Compounds

Benchmark, p-type half-Heulser compound with nominal composition $Nb_{0.75}Ti_{0.25}FeSb$ prepared through an arc-melting and crushing process and consolidated by DC-hot press was provided in dense form by our collaborators. This material has at least two distinct half-Heusler phases with different compositions, and a large fraction of

impurity phases. The microstructure of the benchmark material is shown in Figure 7, highlighting the multiple phases and impurities. The more contrasting phase was identified by EDS to be closely matching the target phase with nominal composition of $Nb_{0.75}Ti_{0.25}FeSb$, whereas the composition of the darker phase was far from what was intended, with a nominal composition of $Nb_{1.12}Ti_{0.33}Fe_{0.75}Sb_{0.8}$. Impurities were confirmed by EDS to be binary phases of Nb – Fe, Fe – Sb, and Nb – Ti, as well as elemental Ti and Nb. The varying compositions of these half-Heusler phase ultimately mean that they have different doping levels, and the overall thermoelectric performance of this material can be expected to be an average of these phases. Furthermore, the impurity phases can be expected to have deleterious effects on the electrical properties of this material.

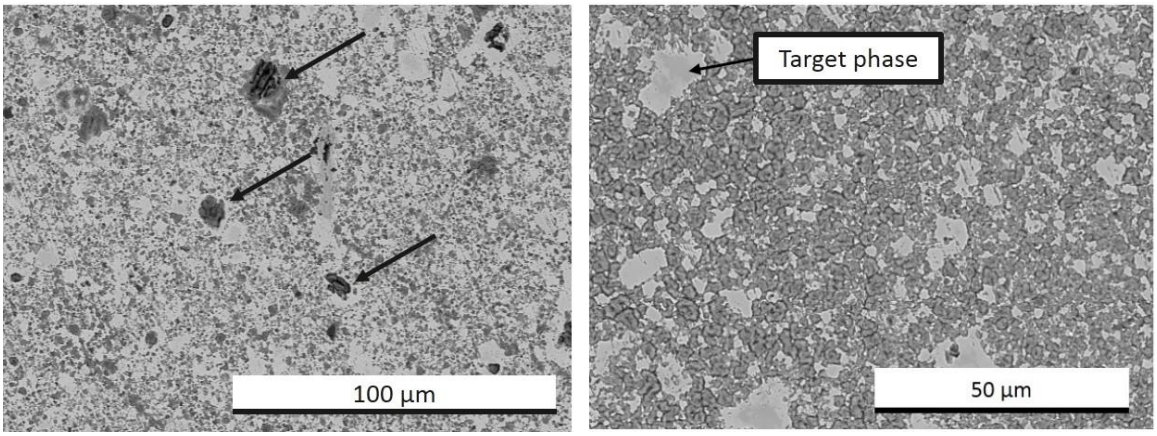

Figure 7: Backscattered scanning electron micrographs of the benchmark p-type half-Heulser compound with nominal composition $Nb_{0.75}Ti_{0.25}FeSb$. Impurities indicated in the left image by arrows include NbFe, FeSb, and NbTi binary phases as well as elemental Ti and Nb. The brighter phase in the right image closely matches the intended composition of $Nb_{0.75}Ti_{0.25}FeSb$ whereas the darker phase was identified by EDS as having a composition of $Nb_{1.12}Ti_{0.33}Fe_{0.75}Sb_{0.8}$.

The as-received powder sintered by SPS has markedly different microstructural features than the material sintered by DC-hot press. A common feature in these materials

are cored structures with a pure-niobium center surrounded by a Nb-rich, Ti- and Sb-poor region. The rest of the material is characterized by dense islands with a composition of $Nb_{0.8}Ti_{0.2}Fe_{1.0}Sb_{1.0}$ surrounded by a less dense, continuous phase with a composition of $Nb_{0.75}Ti_{0.30}Fe_{0.98}Sb_{0.97}$ determined by EDS. These features are shown in Figure 8, along with the corresponding elemental maps generated by an EDS area scan.

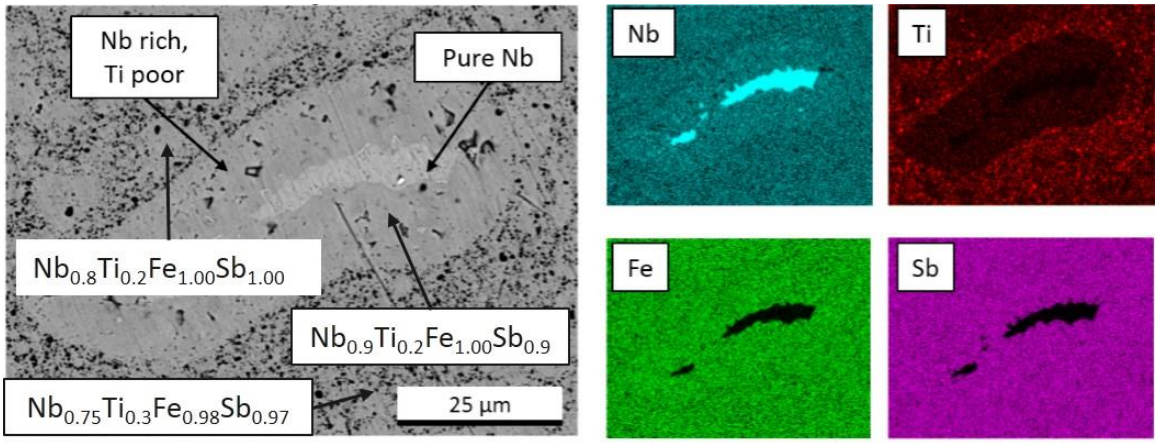

Figure 8: Common features in the as-received NbFeSb based, p-type half-Heusler compound sintered by SPS include regions of pure-niobium surrounded by three regions with distinct compositions and structures. Elemental variations are highlighted by the EDS maps on the right of the image.

Material Refinement: ZrNiSn and NbFeSb Based Compounds

The as-received material synthesized from an arc-melted ingot which was pulverized into a powder by ball milling was first characterized by a solution based, laser-scattering particle size analyzer (LA-950, HORIBA Scientific, Japan). Both n- and p-type powders show a bimodal distribution of particle sizes centered about 1.5 and 15 µm, with particles ranging from about 300 nm to 30 µm and both hard and soft agglomerates as large as a few hundred micrometers (Figure 9). This method of particle size analysis (PSA) relies on the refractive index of the material as well as a precursory knowledge of the shape of the particles (i.e. spherical, faceted, etc.). These two values

were estimated based on typical values of other semiconductors, and thus the PSA presented here is for comparative purposes and is not intended to provide a quantitative value. However, an example of the typical as-received powder morphology is presented in Figure 12, which supports the PSA results. The as-received powders were refined by milling in a high-energy planetary ball mill for an additional twelve hours at 500 rpm. This refining process resulted in both compositions having a unimodal distribution of particle size, as measured by PSA, ranging from about 300 nm to no more than about 20 μm. Mechanically alloyed materials, which are subsequently discussed, show a similar distribution of particle sizes as the refined materials.

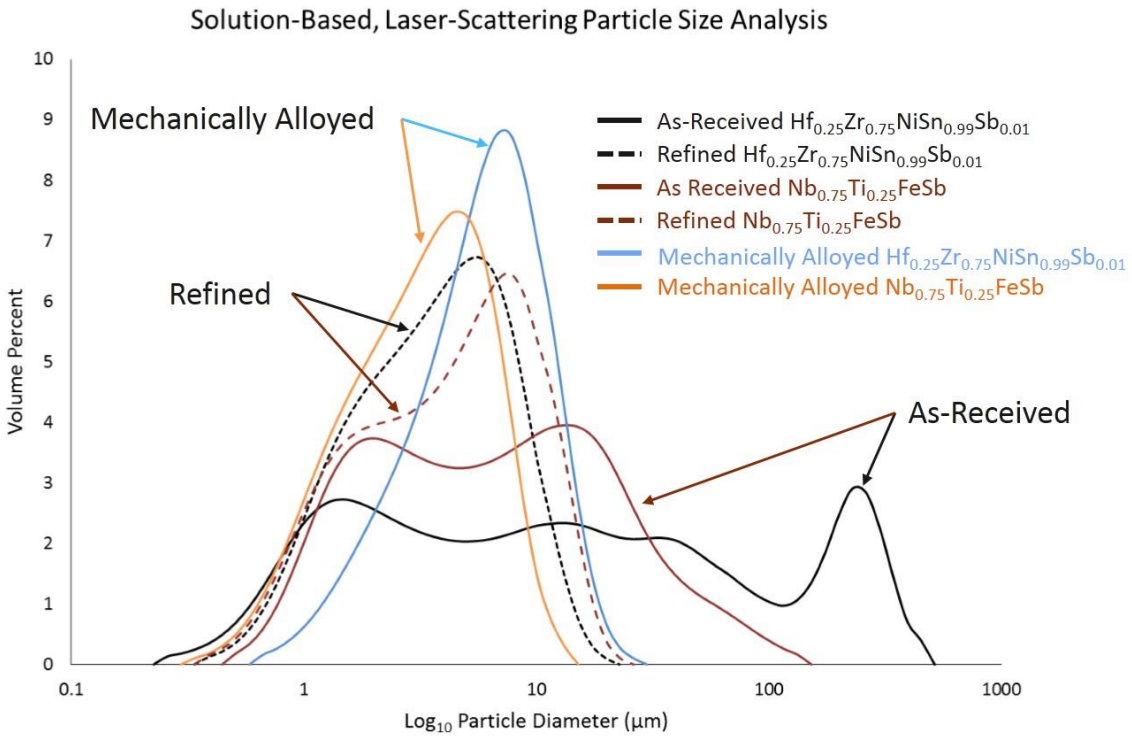

Figure 9: Solution-based, laser-scattering particle size analysis of as-received, refined, and mechanically allowed half-Heusler compounds. Black and crimson curves correspond to the as-received n- and p-type powders respectively. Dashed lines represent those same powders after being refined through an additional ball milling process. The blue and orange lines correspond, respectively, to n- and p-type powders of the same composition which were synthesized through a mechanical alloying process.

As-received and refined, n-type half-Heusler compound with composition of $Hf_{0.25}Zr_{0.75}NiSn_{0.99}Sb_{0.01}$ were investigated for phase-purity by X-Ray diffraction (XRD) (Miniflex 600, Rigaku, Japan). Four separate batches of powder were refined in an attempt to reduce the particle size. There were no impurity phases present within the detectable limits of XRD before or after the additional milling process (Figure 10). However, significant peak broadening suggests that the refined powder is, overall, more disordered, possibly having smaller crystallites, more dislocations, or greater lattice strain than the as-received powder. The microstructure of refined powder sintered by SPS at 975 °C for 10 minutes is shown in Figure 11. This polished and etched surface was used to determine an average grain size of 660 ± 70 nm using the linear intercept method. The same procedure using EDS which was previously used to determine the variance in composition from grain-to-grain in the as-received material was applied to the refined material sintered by SPS (Table 6). However, the average grain size is smaller than the likely interaction volume of the electron beam, making it impossible to isolate a single grain from its neighbors. This leads to an apparent, homogenous composition of $Hf_{0.27}Zr_{0.73}Ni_{1.01}Sn_{0.96}Sb_{0.04}$, meaning that the Hf : Zr ratio is closer in the refined material to the intended composition. However, the measured Sb content is much higher than both the intended composition and what was measured in the as-received material. Interestingly, there is apparently only about 1% excess Ni in the refined material, opposed to the 2 – 3% in the as-received material.

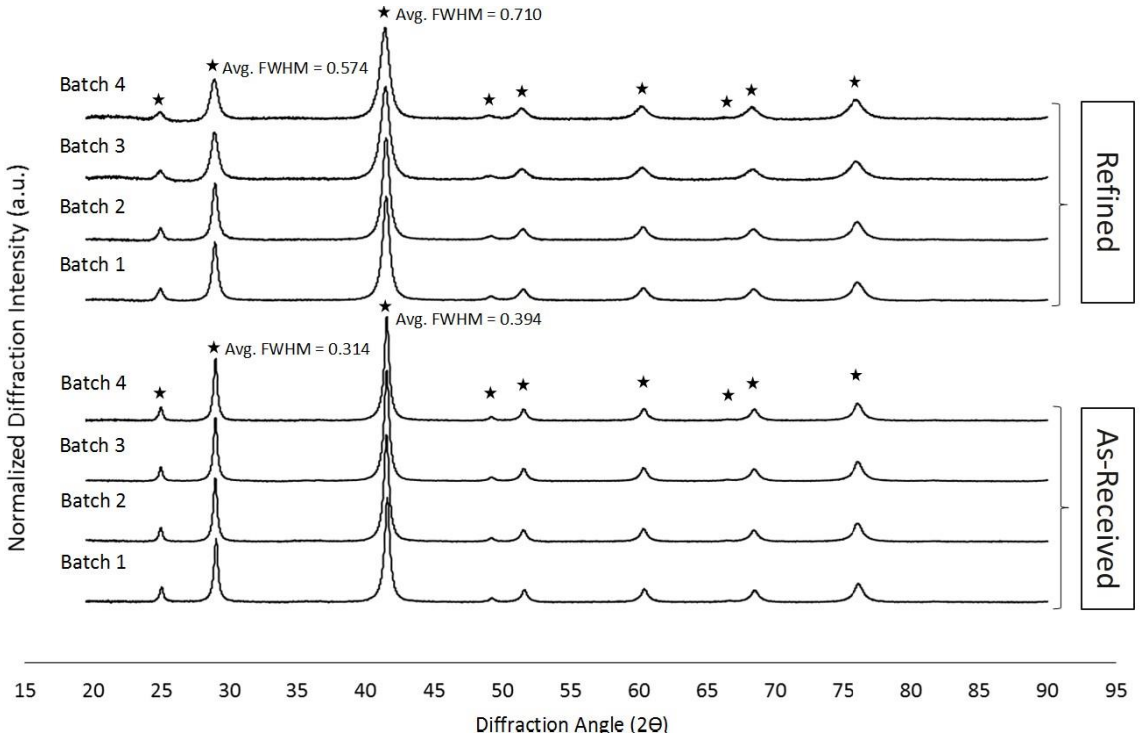

Figure 10: XRD patterns for four separate batches of half-Heusler powders with a composition of $Hf_{0.25}Zr_{0.75}NiSn_{0.99}Sb_{0.01}$ synthesized by arc-melting and crushing both before and after refining. Peaks identified with a star are well-matched to the half-Heusler structure and no impurity phases are detected. Peak broadening, indicated by the average full-width at half-max (FWHM), is a result of the refining process, suggesting a more disordered material.

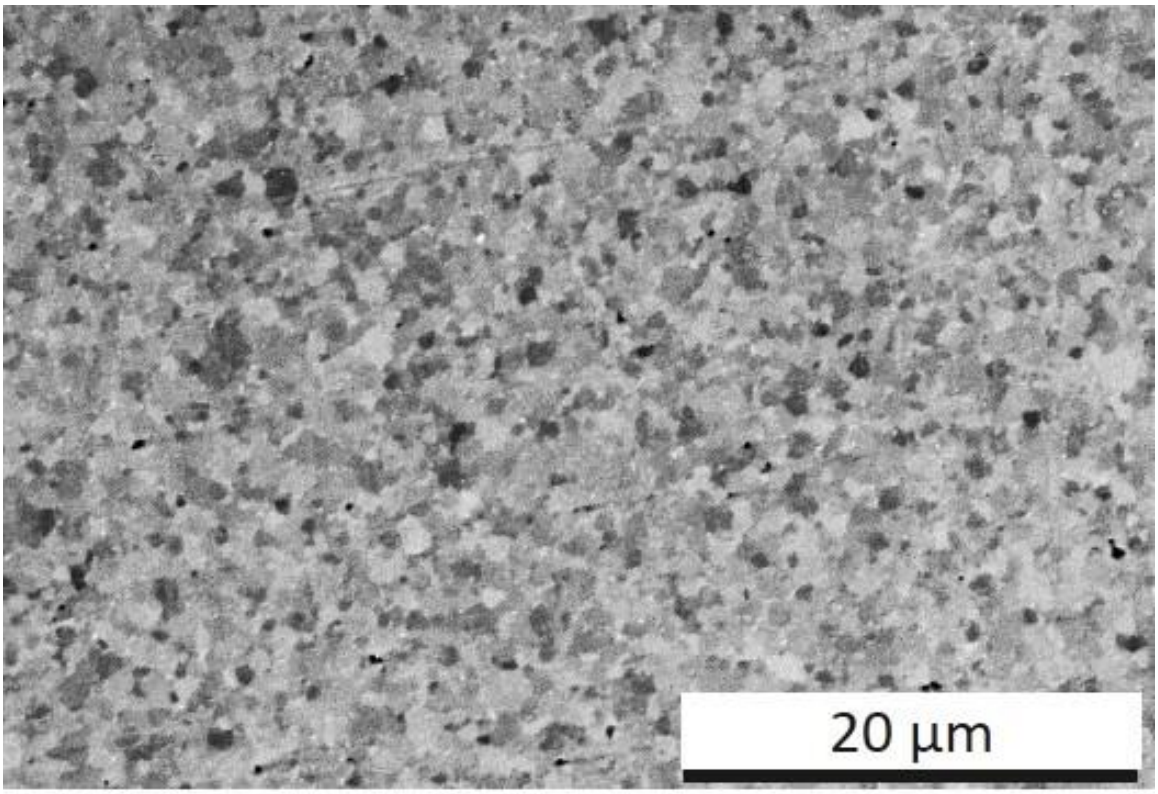

Figure 11: The polished and etched surface of n-type $Hf_{0.25}Zr_{0.75}NiSn_{0.99}Sb_{0.01}$ sintered by SPS using the refined powder. Average grain size is 660 ± 70 nm.

Table 6: The average composition determined by EDS point scans of grains with varying contrast in refined, n-type, half-Heulser compound with a nominal composition of $Hf_{0.25}Zr_{0.75}NiSn_{0.99}Sb_{0.01}$ sintered by SPS. Refer to Figure 11 for an example of grain-to-grain contrast.

Contrast level	Composition determined by EDS point scans				
	Hf	Zr	Ni	Sn	Sb
Black	0.27 ± 0.008	0.73 ± 0.012	1.00 ± 0.011	0.96 ± 0.006	0.04 ± 0.013
Grey	0.26 ± 0.006	0.72 ± 0.010	1.01 ± 0.019	0.96 ± 0.009	0.04 ± 0.017
White	0.27 ± 0.014	0.72 ± 0.014	1.01 ± 0.017	0.96 ± 0.009	0.04 ± 0.014

In addition to having a wide distribution of particle size, the as-received p-type half-Heusler compound with nominal composition of $Nb_{0.75}Ti_{0.25}FeSb$ had a large

quantity of impurity phases. A 10 μm particle with at least three distinct phases, including a Nb – Fe binary phase, is shown in Figure 12. X-Ray diffraction data for four batches of as-received powder is presented in Figure 13, showing peaks from impurity phases. These peaks between 30 and 40 degrees are commonly identified as a Nb_3Sb phase. However, this conclusion is not supported by EDS which does not identify any Nb – Sb binary phases, and the peaks can be explained equally well by the presence of a combination of pure Nb, Ti, Fe and Sb, or by Ti_3Sb, $NbTi_4$, or Nb_5Sb_4, Nb_6Fe_7, $NbFe_2$, or $FeSb_4$ phases, any of which are present in the Nb-Fe-Sb ternary phase diagram.[55]

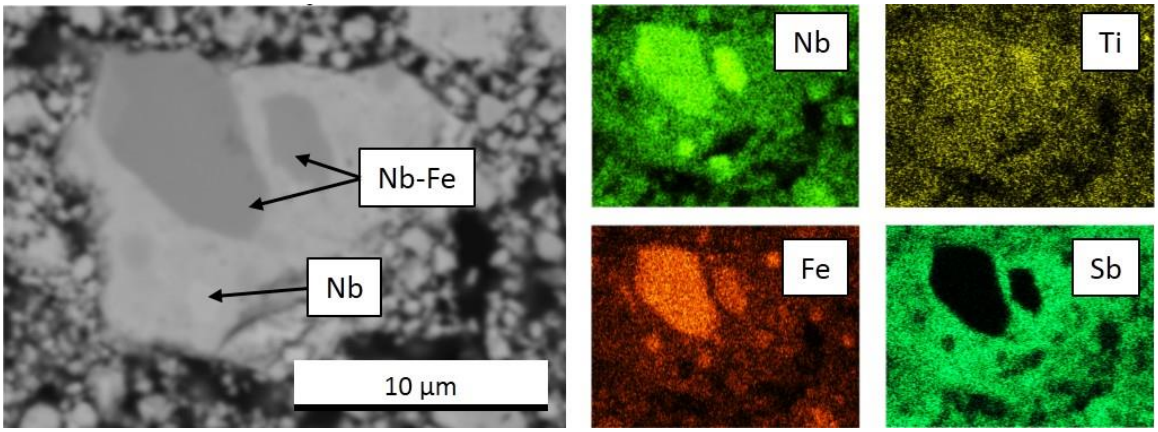

Figure 12: $Nb_{0.75}Ti_{0.25}FeSb$ powder mounted in resin and cross-sectioned. The backscattered electron micrograph (left) shows a mix of large and small particles and at least three distinct phases are easily identified. Corresponding elemental maps generated by EDS show a Nb-Fe phase, as well as regions of unmixed Nb and Ti.

The refining process appears to have eliminated the largest particles in the as-received, p-type powder, but did not significantly reduce the particle size measured by PSA (Figure 9). However, the most prominent result of the refining process is that it seemingly eliminated impurity phases by alloying pure metals and binary phases into a homogenous half-Heusler material, evidenced by the XRD patterns in Figure 13. Four separate batches of as-received powder with composition of $Nb_{0.75}Ti_{0.25}FeSb$ were milled

for an additional twelve hours at 500 rpm, and in each case, peaks associated with impurity phases were eliminated and the XRD pattern of the refined powder is well matched to the half-Heusler structure.

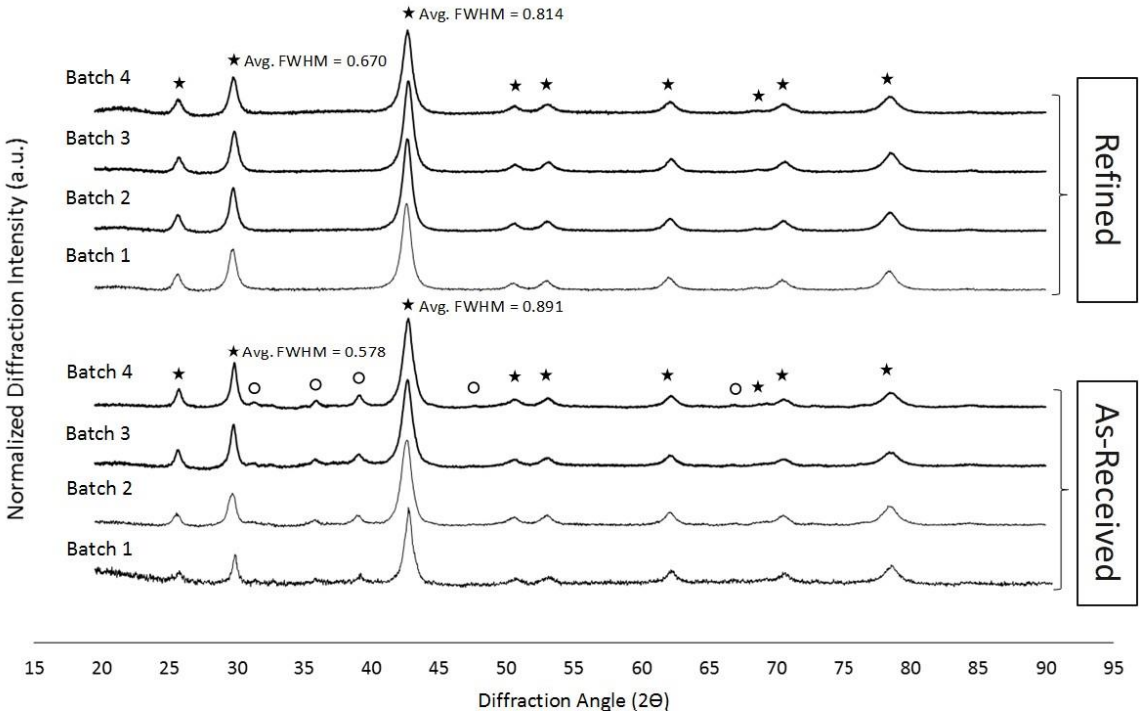

Figure 13: XRD patterns for four separate batches of half-Heusler powders with a composition of $Nb_{0.75}Ti_{0.25}FeSb$ synthesized by arc-melting and crushing both before and after refining. Peaks identified with a star are well-matched to the half-Heusler structure and those labeled with an open circle indicate the presence of one or more impurity phases. No significant amount of peak broadening, indicated by the average full-width at half-max (FWHM), suggests that the refining process had no effect on the particle size or structure of this material. However, the refining process eliminated the presence of any peaks from an impurity phase.

The as-received and refined material, both sintered by SPS at 975 °C for 10 minutes, are compared in Figure 14. Characteristic of the as-received material, dense islands are surrounded by a continuous phase with a different composition, and impurities in the form of metallic inclusions are prevalent. The refined material has a homogenous distribution of grains on the order of about 3 – 10 μm. A more detailed look at the refined

material in Figure 15 shows that regions of sub-micrometer grains separate larger grains. Although there is grain-to-grain contrast in these images, there is no significant compositional variation detectable by EDS (Table 7). This suggests that the refined material has a homogenous composition of about $Nb_{0.77}Ti_{0.23}Fe_{1.01}Sb_{0.99}$, which is very close to the intended composition of $Nb_{0.75}Ti_{0.25}FeSb$. Unlike the as-received material, whose thermoelectric performance will be influenced by the presence of at least three distinct compositions of half-Heusler, the thermoelectric properties of the refined material should accurately represent the single phase material with 25% substitution of Ti for Nb.

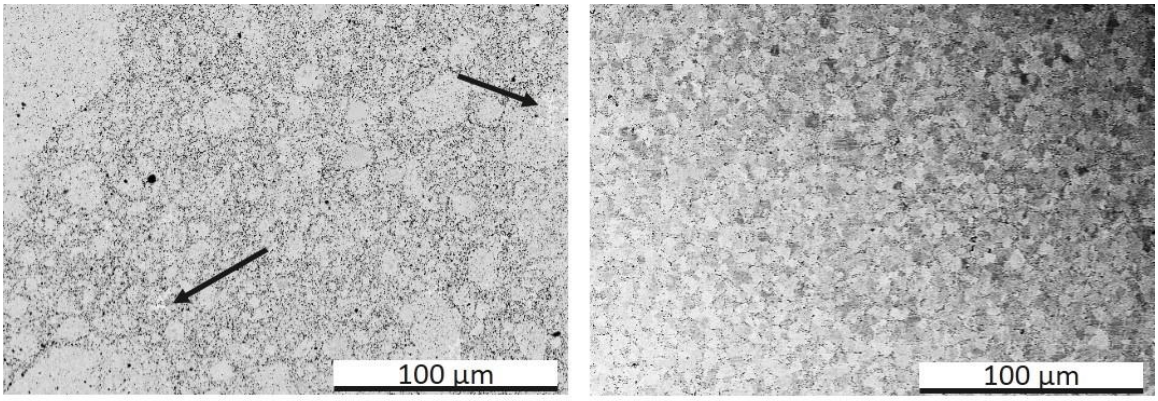

Figure 14: As-received (left) material is compared to refined material (right) of p-type $Nb_{0.75}Ti_{0.25}FeSb$ composition. Arrows indicate regions of pure, unmixed metal in the as-received material, evidenced by high contrast in the SEM image. As-received material shows dense islands surrounding by a continuous phase with different composition, whereas the refined material shows a more homogenous distribution of grain size and composition.

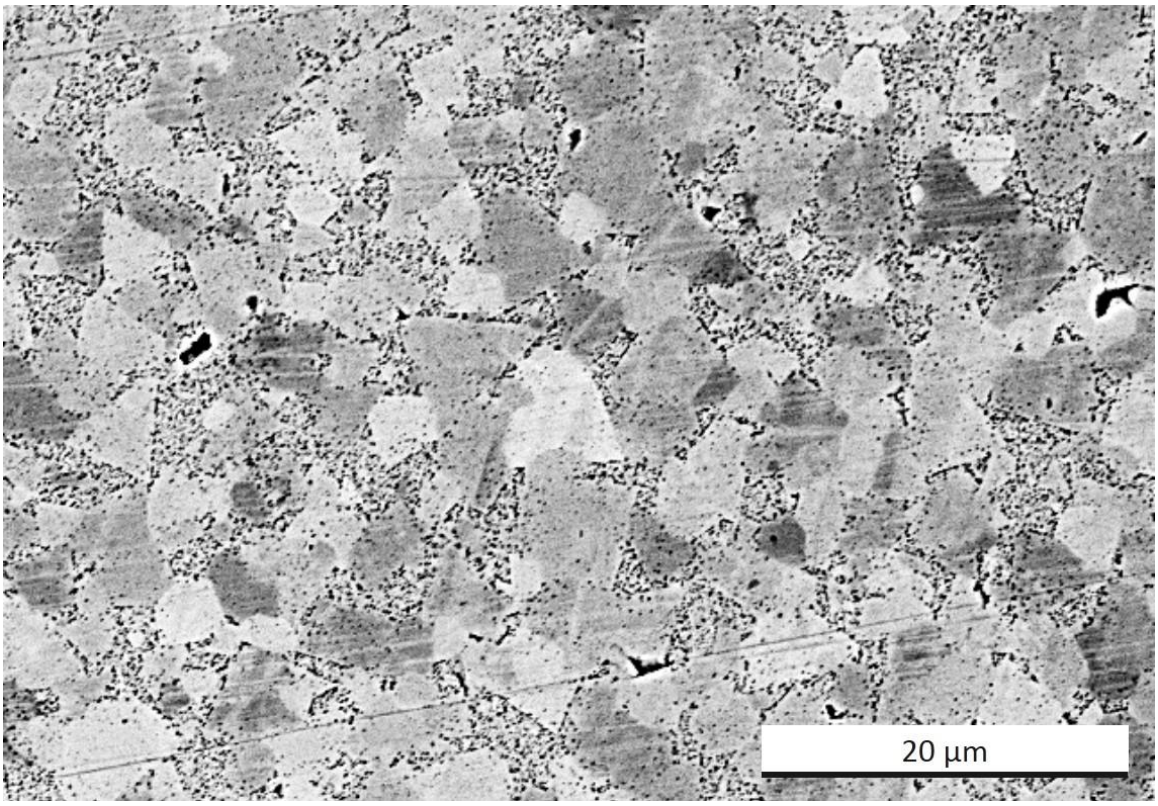

Figure 15: Backscattered SEM image of a polished and etched surface of refined, p-type $Nb_{0.75}Ti_{0.25}FeSb$ material sintered by SPS. Grains on the order of 3 – 10 µm are surrounding by sub-micrometer grains.

Table 7: The average composition determined by EDS point scans of grains with varying contrast in refined, p-type, half-Heulser compound with a nominal composition of $Nb_{0.75}Ti_{0.25}FeSb$ sintered by SPS. Refer to Figure 21 for an example of grain-to-grain contrast.

Contrast level	Composition determined by EDS point scans			
	Nb	Ti	Fe	Sb
Black	0.77 ± 0.010	0.23 ± 0.015	1.01 ± 0.008	0.99 ± 0.006
Grey	0.77 ± 0.015	0.23 ± 0.023	1.01 ± 0.006	0.99 ± 0.010
White	0.76 ± 0.011	0.25 ± 0.020	1.01 ± 0.009	0.99 ± 0.005

Although no impurity phases were detected in the refined powder by XRD analysis, an Fe – Sb binary phase was present in the refined material sintered by SPS. This phase in shown in Figure 16 surrounding grains of half-Heusler. Impurity peaks in the XRD patterns of sintered pellets are well matched to an Fe - Sb phase (Space group 194, $P6_3/mmc$). This structure was confirmed by EBSD (Figure 17), which shows this phase to be present as large grains as well as distributed as particles at grain boundaries and grain interiors. Although impurity phases can generally be expected to have negative effects on the electrical properties of half-Heusler compounds, these hexagonal, Fe – Sb phases have the potential to contribute to phonon scattering, and possibly lower the thermal conductivity of this material.

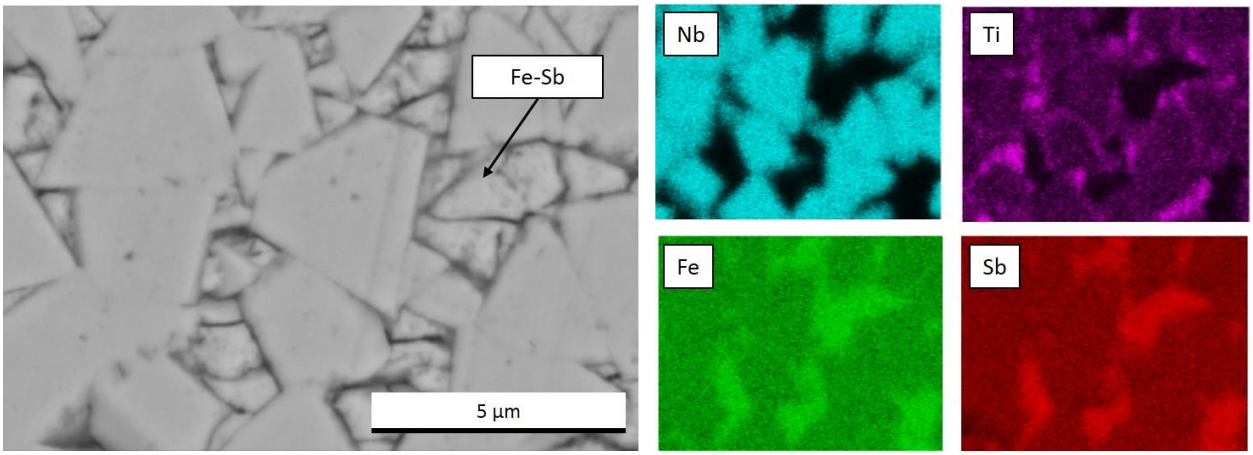

Figure 16: Backscattered electron micrograph and its corresponding elemental maps of a dense pellet consolidated from refined $Nb_{0.75}Ti_{0.25}FeSb$ powder showing half-Heusler grains on the order of 3 – 5 µm, surrounded by an Fe – Sb secondary phase.

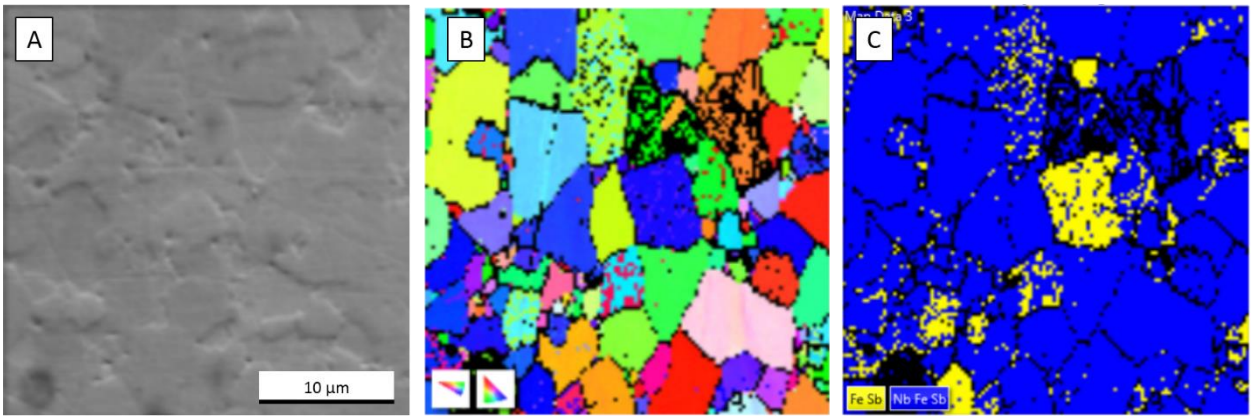

Figure 17: (A) Secondary electron micrograph of a dense pellet consolidated from refined $Nb_{0.75}Ti_{0.25}FeSb$ powder and (B) its corresponding EBSD pole-figure showing random crystallographic orientation. (C) The corresponding phase map shows the half-Heusler phase ($F\bar{4}3m$) in blue and the FeSb phase ($P6_3/mmc$) in yellow.

Mechanical Alloying: ZrNiSn, NbFeSb, and NbCoSn Based Compounds

The most popular methods of producing useful quantities of fine-grained half-Heusler powders have been to cast an ingot using arc- or induction-melting, followed by pulverizing the ingot in a mill to produce a powder. Other methods to produce homogenous half-Heusler ingots have included lengthy solid state reactions, optical floating zone melting, and microwave heating.[11] Although mechanical synthesis techniques have been used successfully to produce other thermoelectric materials such as various bismuth telluride and silicon germanium compositions, it has shown only moderate success when applied to half-Heuslers.[11,35,36,45,46] The present work seeks to demonstrate mechanical alloying as a rapid, single-step mechanical synthesis route for producing useful quantities of single-phase, half-Heusler nano-powders.

First, n-type ZrNiSn based half-Heusler compounds were synthesized with the same nominal composition as the current work, as well as some other compositions which have been reported to have high thermoelectric performance. X-Ray diffraction patterns for three separate batches of mechanically alloyed powder is presented in Figure

18. All powders were mechanically alloyed at 500 rpm for up to 76 hours, and interrupted periodically to take a sample of powder for XRD. Peaks attributable to the formation of the half-Heusler phase were evident in each batch, but even after 76 hours of milling, a single phase powder was not obtained.

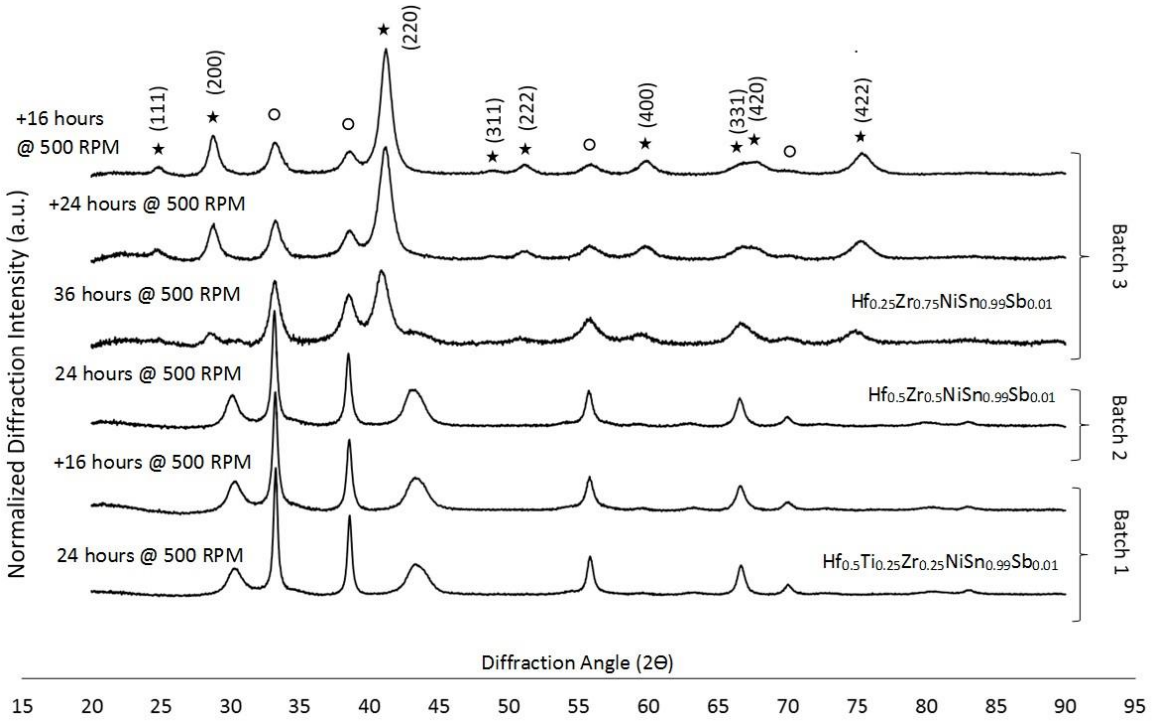

Figure 18: Powder XRD patterns for n-type half-Heusler compounds with nominal compositions of $Hf_{0.50}Ti_{0.25}Zr_{0.25}NiSn_{0.99}Sb_{0.01}$ (Batch 1), $Hf_{0.5}Zr_{0.5}NiSn_{0.99}Sb_{0.01}$ (Batch 2), and $Hf_{0.25}Zr_{0.75}NiSn_{0.99}Sb_{0.01}$ (Batch 3). Peaks matched to the half-Heusler structure are labeled with a star and indexed. Impurity peaks are labeled with an open circle and are likely from unmixed Hf or Zr.

Material sintered from mechanically synthesized $Hf_{0.25}Zr_{0.75}NiSn_{0.99}Sb_{0.01}$ contained two distinct phases of half-Heusler compositions and regions of unmixed metals (Figure 19). According to EDS, Ni and Sn were homogenously distributed throughout the material, but where Zr was present Hf was not, and vis-versa. This suggests that a HfNiSn / ZrNiSn, half-Heusler / half-Heusler composite was made. This

further supports the belief that Hf- and Zr-containing half-Heusler compounds cannot be synthesized by this type of ball milling process.

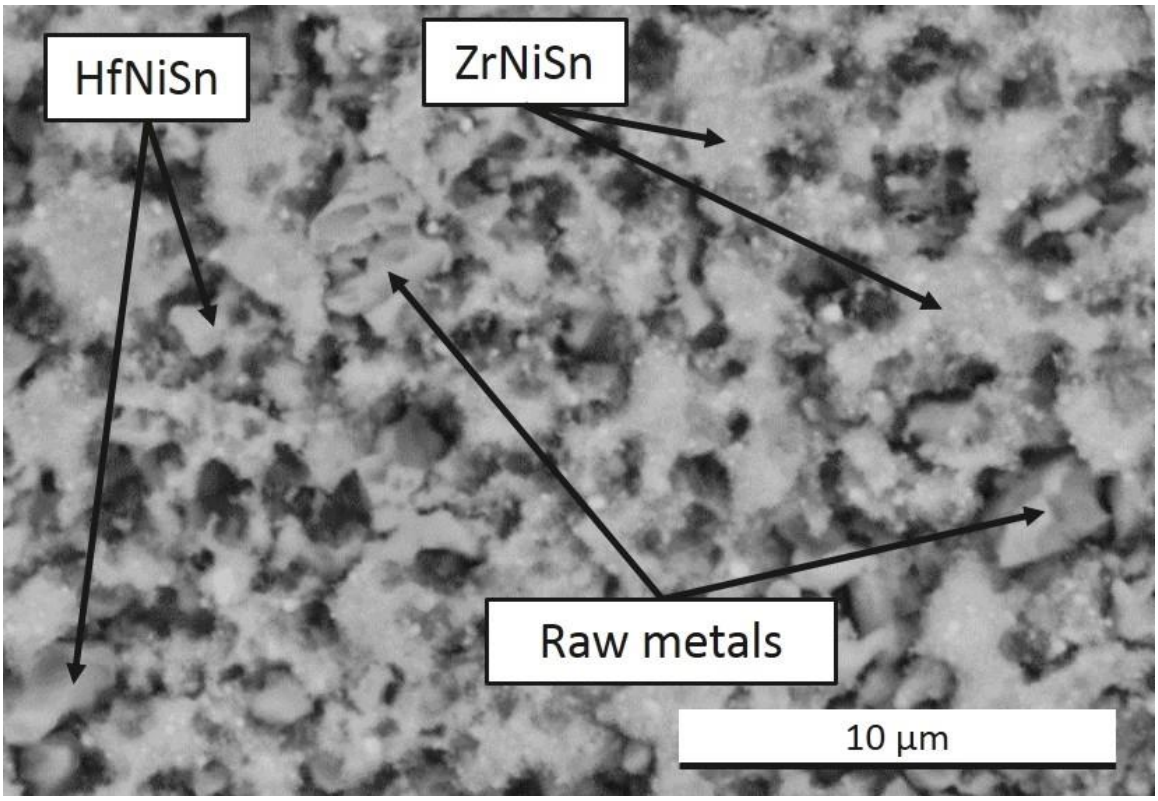

Figure 19: Backscattered SEM image of a mechanically synthesized, half-Heusler compound with nominal composition of $Hf_{0.25}Zr_{0.75}NiSn_{0.99}Sb_{0.01}$ sintered by SPS. Hf and Zr were not successfully alloyed to form a single phase half-Heulser compound.

Next, p-type, NbFeSb based half-Heusler compounds with nominal compositions of $Nb_{0.75}Ti_{0.25}FeSb$, $Nb_{0.96}Ti_{0.04}FeSb$, and $Nb_{0.88}Hf_{0.12}FeSb$ were mechanically synthesized. Again, Hf-containing half-Heusler compositions of a single-phase could not be synthesized by mechanical alloying. The structure of the mechanically synthesized $Nb_{0.88}Hf_{0.12}FeSb$ sintered by SPS is presented in Figure 20, showing that Hf was not incorporated into the half-Heusler structure and is segregated at grain boundaries. This material had an essentially zero Seebeck coefficient and exceptionally low electrictal conductivity at room temperature and was not pursued any further. However, single

phase, Ti-containing half-Heusler compounds were successfully synthesized by twelve hours of milling at 500 rpm. Typical XRD patterns for mechanically synthesized powders are shown in Figure 21 and are compared to the as-received and refined materials. As in the refined material, the FeSb phase was detectable by XRD after sintering. However, this phase was not evident in SEM (Figure 22). Furthermore, mechanically synthesized $Nb_{0.75}Ti_{0.25}FeSb$ based compounds had a much finer grain size than the as-received or the refined material, with an average grain size of 440 ± 70 nm.

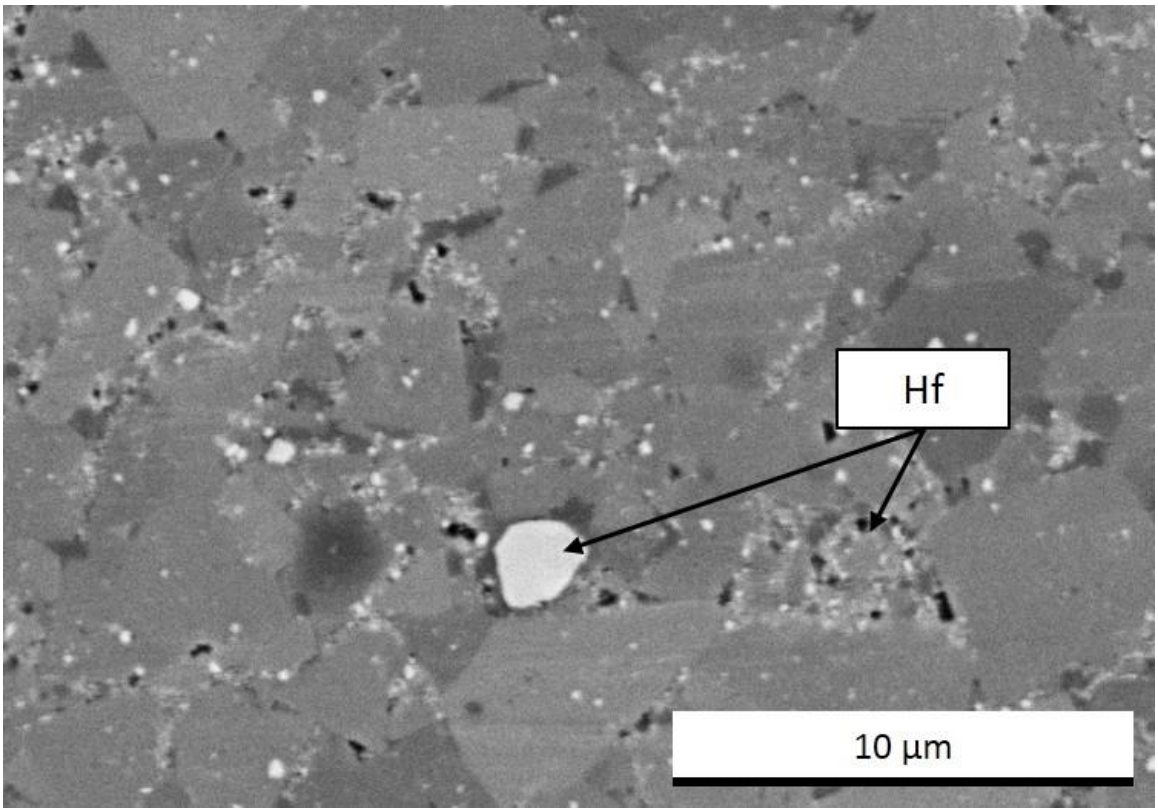

Figure 20: $Nb_{0.88}Hf_{0.12}FeSb$ half-Heusler prepared by mechanical synthesis and SPS. Hf was not incorporated into the structure and is evident at grain boundaries.

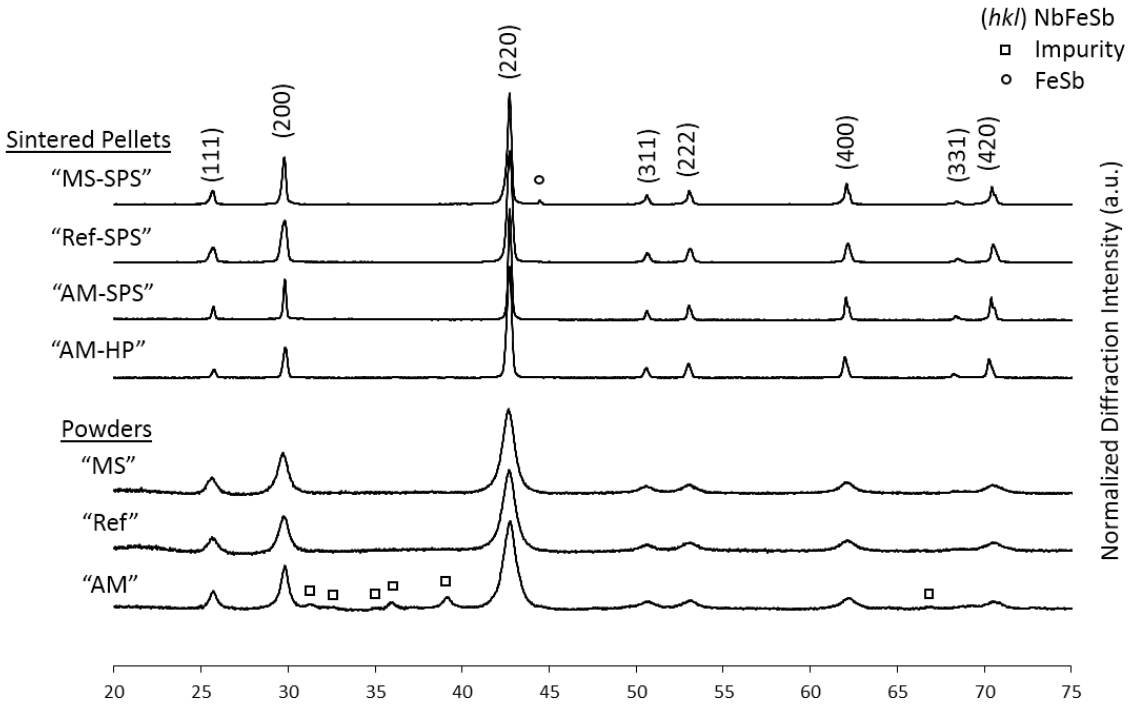

Figure 21: X-Ray diffraction patterns for arc-melted and crushed powders (AM), these same powders refined through extra ball milling (Ref), and powders which were mechanically synthesized (MS). Arc-melted and crushed powders were consolidated by DC-hot press (AM-HP) and by SPS (AM-SPS). Refined powders and mechanically synthesized powders were consolidated by SPS (Ref-SPS and MS-SPS). Peaks of the ternary NbFeSb compound are indexed and impurity phases are labeled.

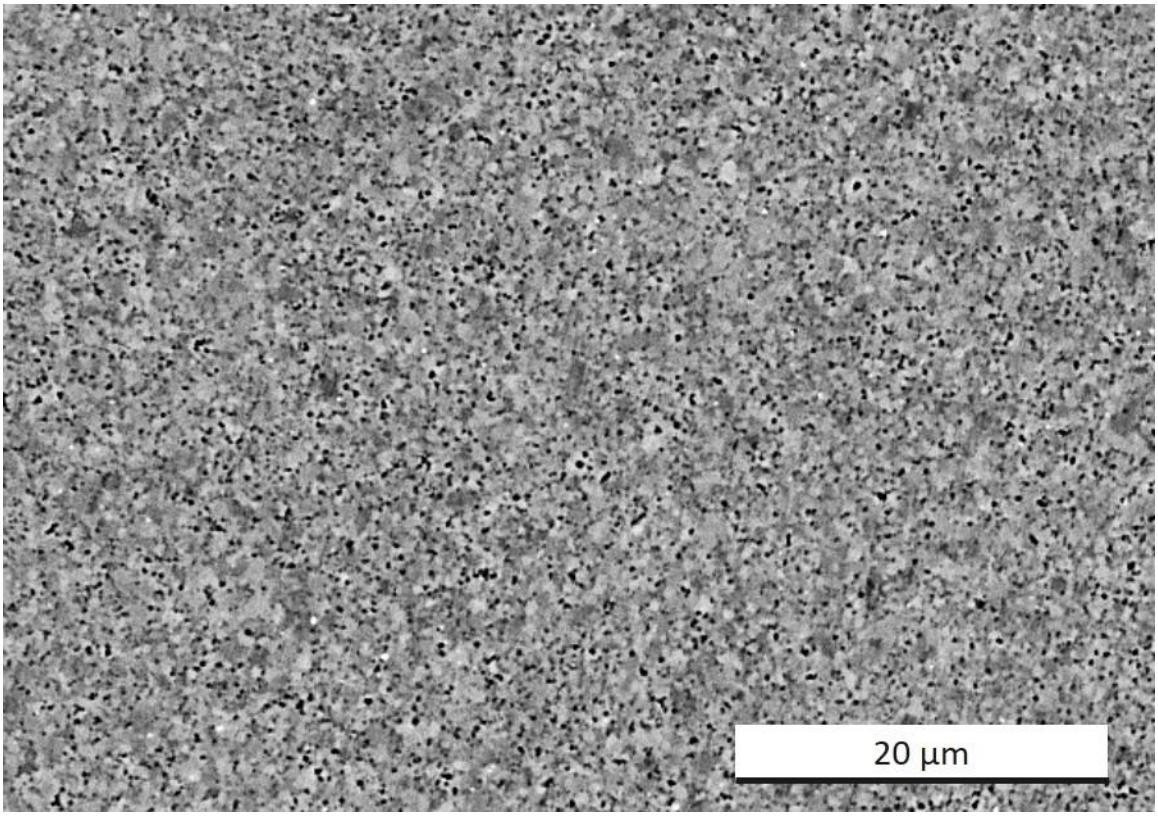

Figure 22: Backscattered SEM image of the polished and etched surface of mechanically synthesized $Nb_{0.75}Ti_{0.25}FeSb$ compound sintered by SPS. Average grain size is 440 ± 70 nm determined by the linear intercept method. Apparent porosity is exaggerated by the etching process.

Finally, single phase, NbCoSn based half-Heusler compounds were synthesized by twelve hours of mechanical alloying at 500 rpm. Typical XRD patterns of these powders and the pellets sintered by SPS using these powders are presented in Figure 23. A small amount of an impurity phase was detected in the sintered pellets, possibly a Nb_3Sn phase, however, no impurities were evident in SEM. A fractured surface and a polished and etched surface of the $NbCoSn_{0.9}Sb_{0.1}$ material sintered by SPS is shown in Figure 24, revealing an average grain size of 300 ± 40 nm determined by the linear intercept method.

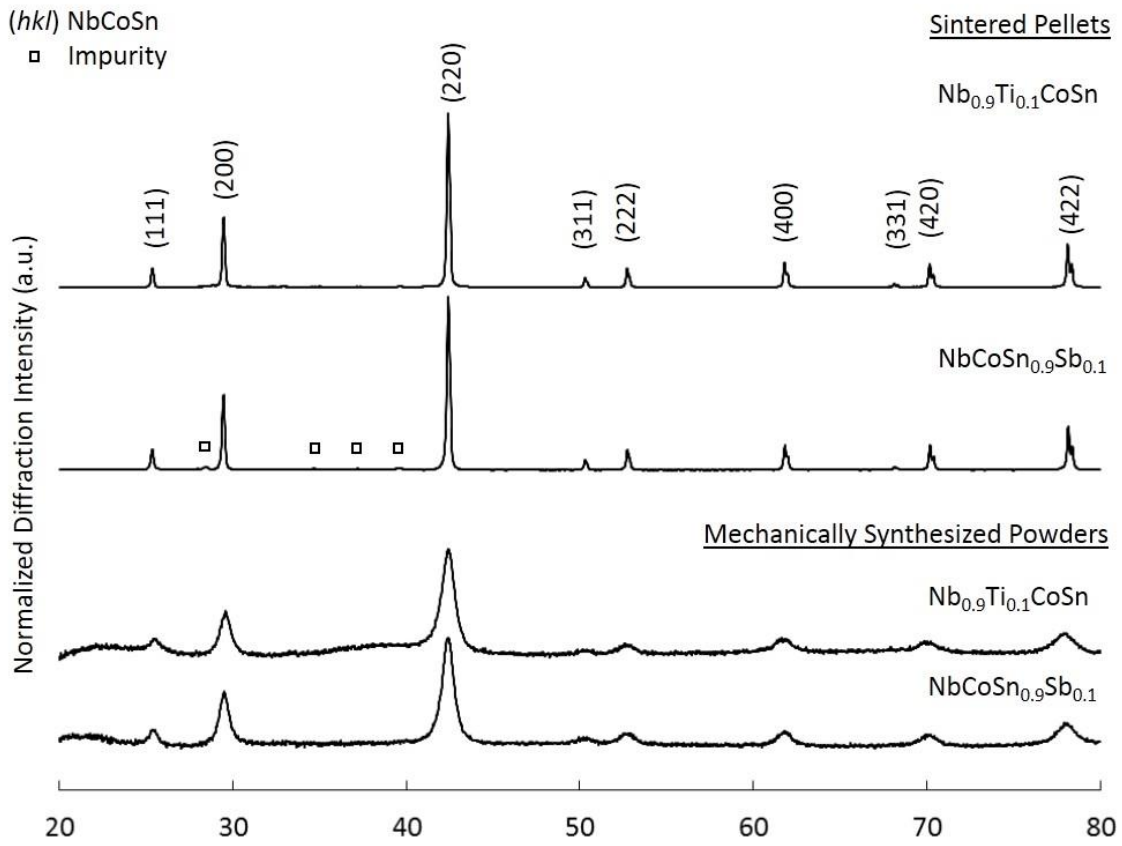

Figure 23: Typical X-Ray diffraction patterns of mechanically synthesized powders (bottom) are compared to those of the sintered pellets consolidated from the same powders (top). Characteristic peaks of the half-Heusler structure NbCoSn are indexed and impurity phases are labeled.

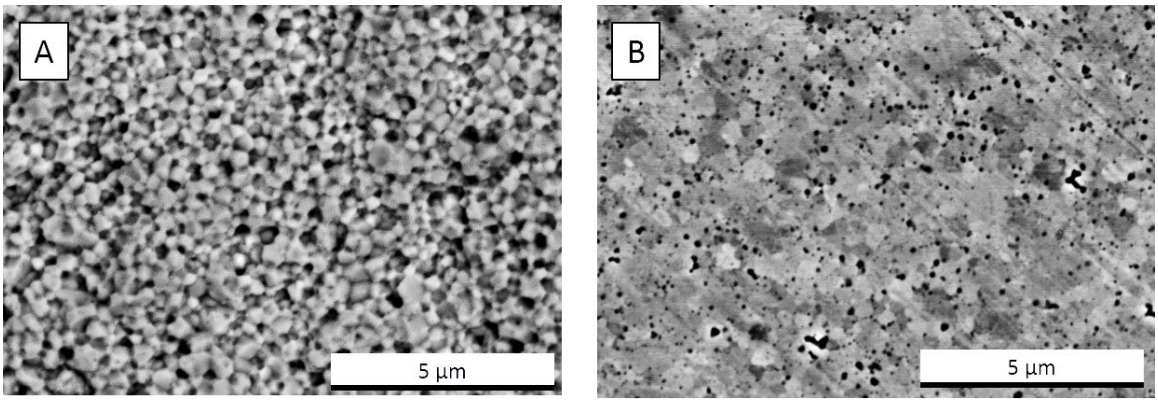

Figure 24: Scanning electron micrographs of (A) a fractured surface and (B) the polished and etched surface of the n-type $NbCoSn_{0.9}Sb_{0.1}$. Average grain size is 300 ± 40 nm.

Thermoelectric Performance

The performance of a thermoelectric device relies directly on the intrinsic material property known as its thermoelectric figure of merit (*ZT*), denoted:

$$ZT = \frac{S^2 \sigma}{\kappa} T$$

where *S* is the Seebeck coefficient ($V \cdot K^{-1}$), σ is the electrical conductivity ($\Omega^{-1} \cdot m^{-1}$), κ is the thermal conductivity ($W \cdot m^{-1} \cdot K^{-1}$), and *T* is the absolute temperature at which the properties are measured (*K).* These properties were measured for each the benchmark, as-received, refined, and mechanically synthesized ZrNiSn, NbFeSb, and NbCoSn based half-Heusler compounds. For each material the ZT and power factor ($S^2\sigma$) is calculated, and the lattice thermal conductivity is separated from the total thermal conductivity assuming a constant Lorenz number of $2.44 \cdot 10^{-8}$ ($W\ \Omega\ K^{-2}$) across all temperatures.

Beginning with the n-type half-Heusler compound with nominal composition of $Hf_{0.25}Zr_{0.75}NiSn_{0.99}Sb_{0.01}$, the highest performance is realized by the as-received material sintered by SPS, with a ZT up to 10% higher than the same powder sintered by DC-hot press (Figure 25). Despite having a much finer grain size and more homogenous microstructure, the ZT of the refined material is about 10% lower than the benchmark. Although high figures of merit have been achieved in multi-phase half-Heusler composites, the mechanically alloyed material here shows very poor performance. There is no significant difference in performance of this material depending on the temperature at which it was sintered or the time spent at temperature in the SPS, so only one curve is shown for each material. The higher ZT is a direct result of the higher power factor achieved by the as-received material (Figure 26), which is up to 30% higher than the refined material at low temperatures, and up to 20% higher than the benchmark at

intermediate temperatures. This is due to the as-received material having a somewhat higher Seebeck coefficient (Figure 27) and nearly the same electrical conductivity (Figure 28) when compared to the benchmark material. The as-received material also benefits from a slightly lower thermal conductivity than the benchmark material (Figure 29), ultimately due to a lower contribution from the lattice component of thermal conductivity (Figure 30).

The ultimate goal of the refining process was to reduce the average grain size and lower the lattice thermal conductivity by introducing more phonon-scattering centers in the form of grain boundaries. This goal was accomplished, and there is a significant reduction in lattice thermal conductivity in the refined material. However, because of the characteristically high electrical conductivities in half-Heusler compounds, there is a significant contribution to the total thermal conductivity from electronic charge carriers. Because the refined material has a much higher electrical conductivity than the as-received material, its total thermal conductivity is significantly higher, and thus it did not reach as high a ZT as the other materials. The reason for the increase in electrical conductivity resulting from the refining process is not immediately known. However, the diminished Seebeck coefficient, and the increase in both electrical and thermal conductivities can all be attributed to an increase in the total number of charge carriers. As evidenced by the EDS analysis of the refined material, it is possible that excess Sb was alloyed into the half-Heusler compound during the refining process, increasing the doping level. What is clear though, is that the finer grain structure was effective at reducing the lattice thermal conductivity. If the degraded electrical properties of the refined material are in fact a result of increased Sb content, than having a greater control

over the starting composition could help to regain the high power factor. This, combined with the reduction of lattice thermal conductivity by the refining process, could lead to large gains in ZT.

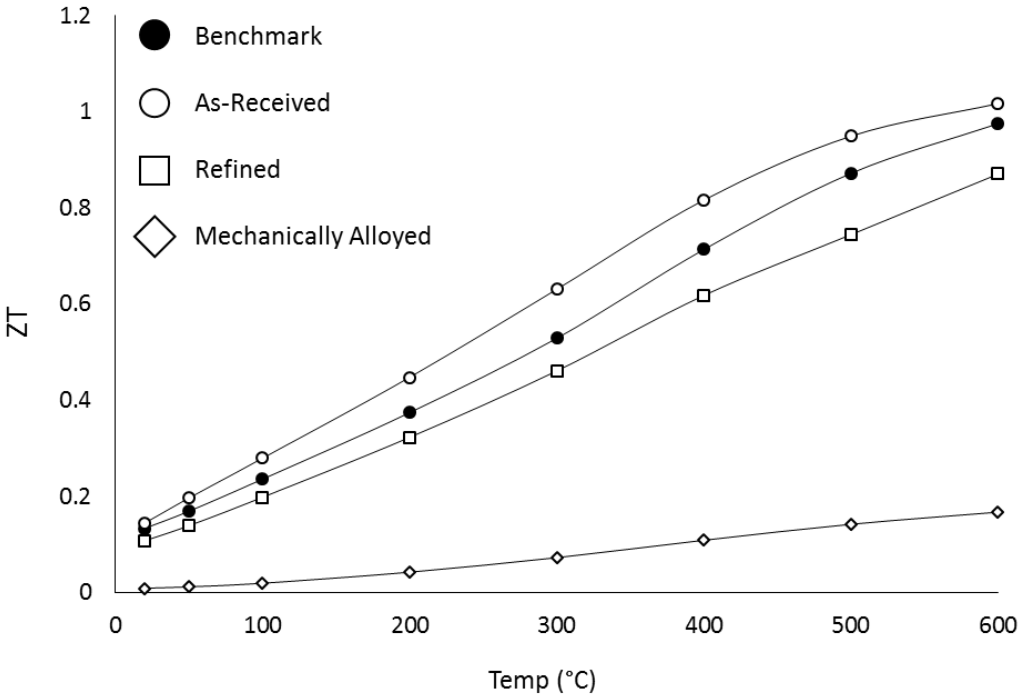

Figure 25: Thermoelectric figure of merit for n-type half-Heusler compound with nominal composition of $Hf_{0.25}Zr_{0.75}NiSn_{0.99}Sb_{0.01}$. Solid lines are a guide for the eye.

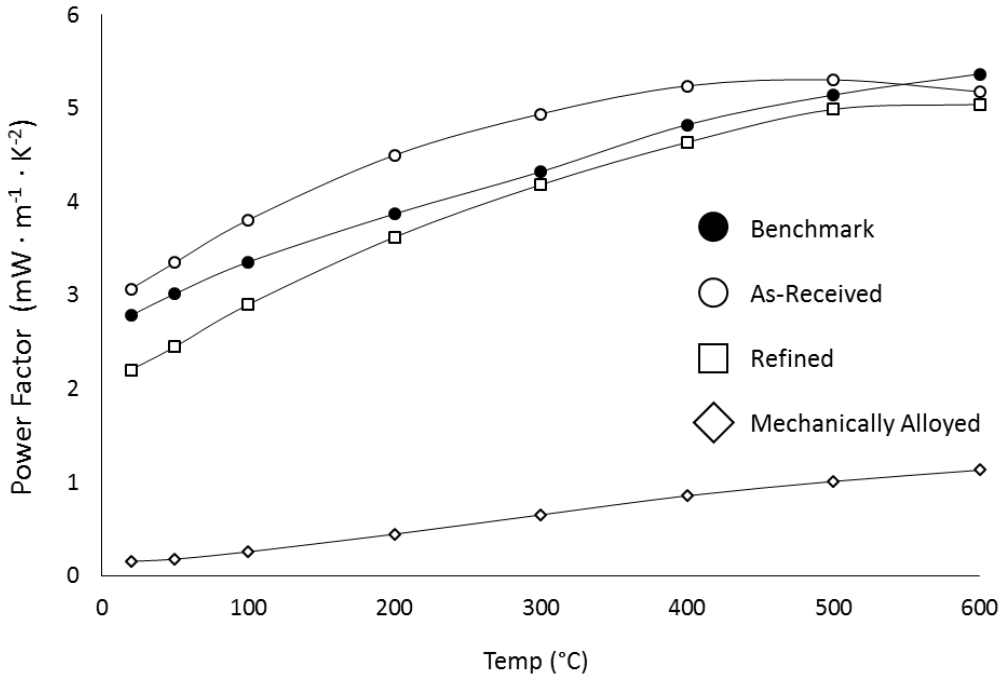

Figure 26: The calculated power factor ($S^2\sigma$) for n-type half-Heusler compound with nominal composition of $Hf_{0.25}Zr_{0.75}NiSn_{0.99}Sb_{0.01}$. Solid lines are a guide for the eye.

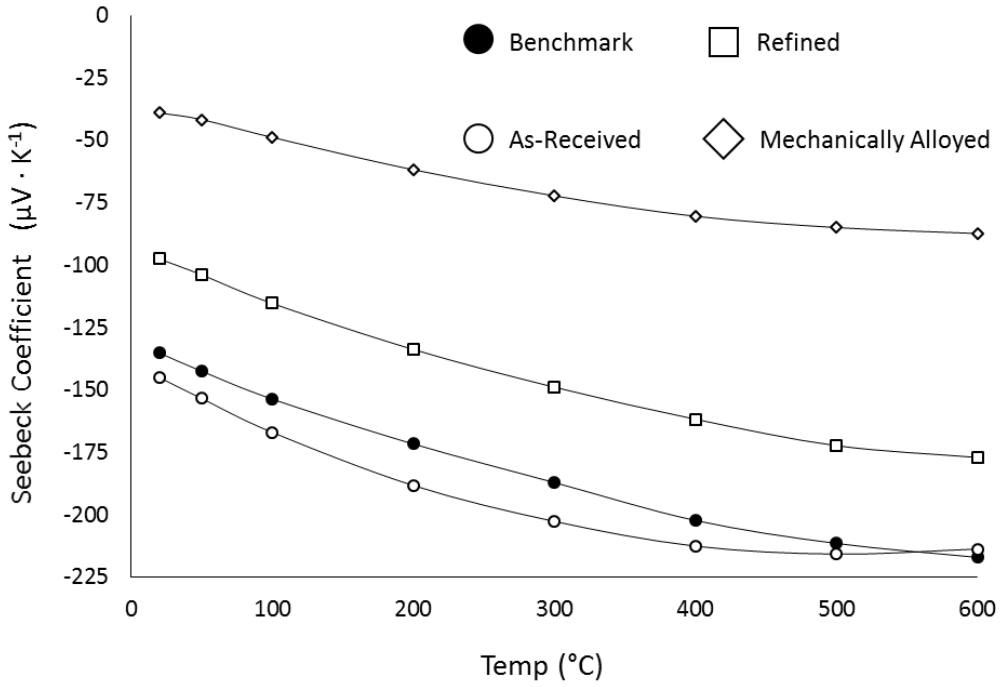

Figure 27: The Seebeck coefficient for n-type half-Heusler compound with nominal composition of $Hf_{0.25}Zr_{0.75}NiSn_{0.99}Sb_{0.01}$. Solid lines are a guide for the eye.

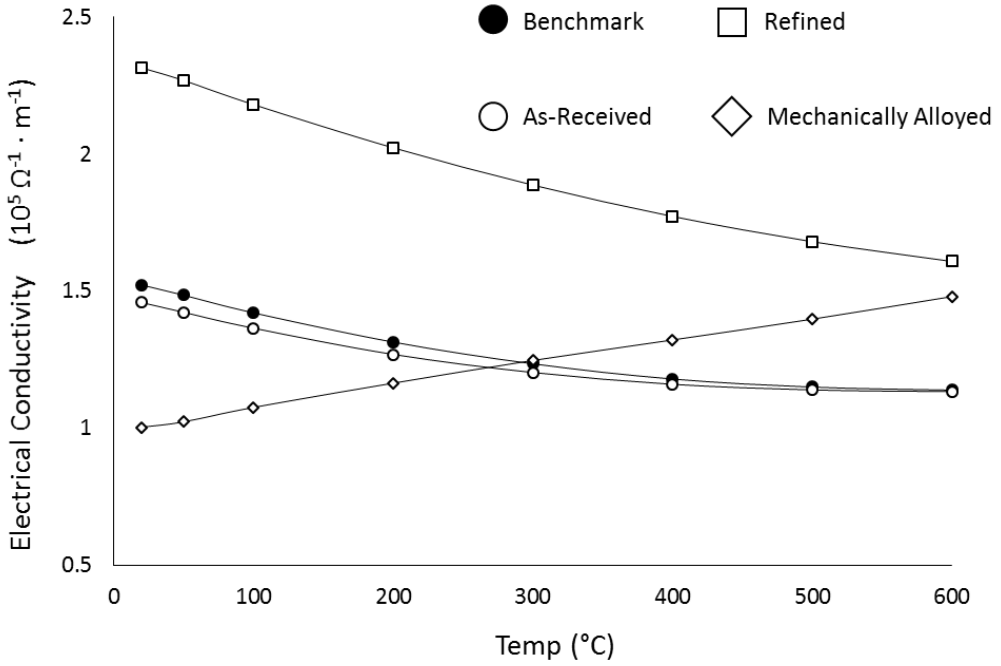

Figure 28: The electrical conductivity for n-type half-Heusler compound with nominal composition of $Hf_{0.25}Zr_{0.75}NiSn_{0.99}Sb_{0.01}$. Solid lines are a guide for the eye.

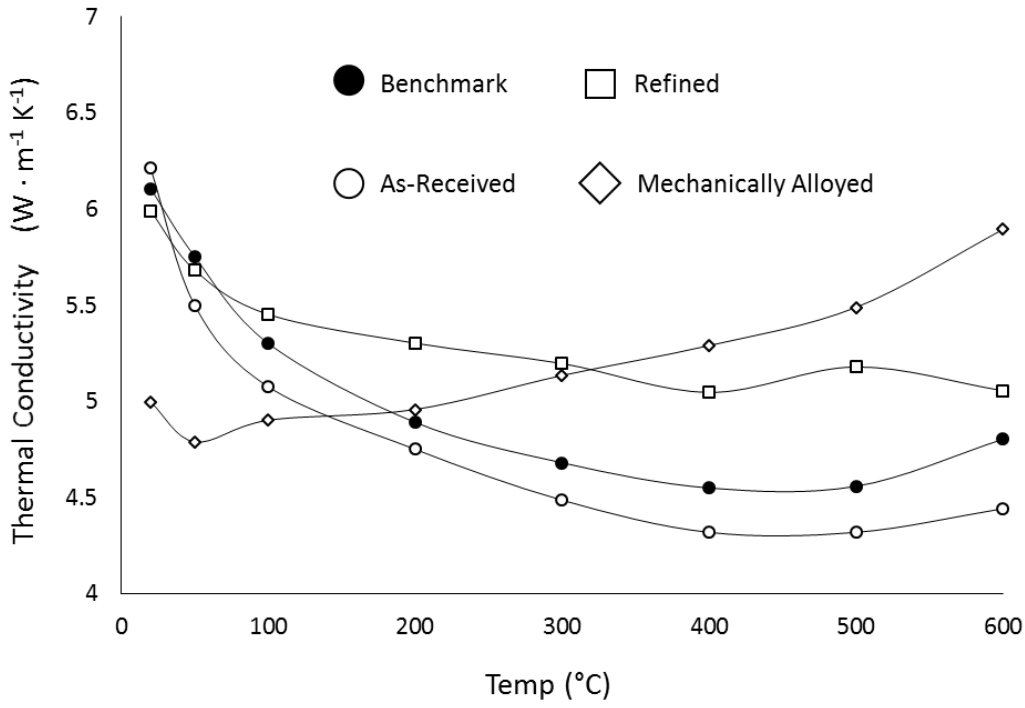

Figure 29: The total thermal conductivity for n-type half-Heusler compound with nominal composition of $Hf_{0.25}Zr_{0.75}NiSn_{0.99}Sb_{0.01}$. Solid lines are a guide for the eye.

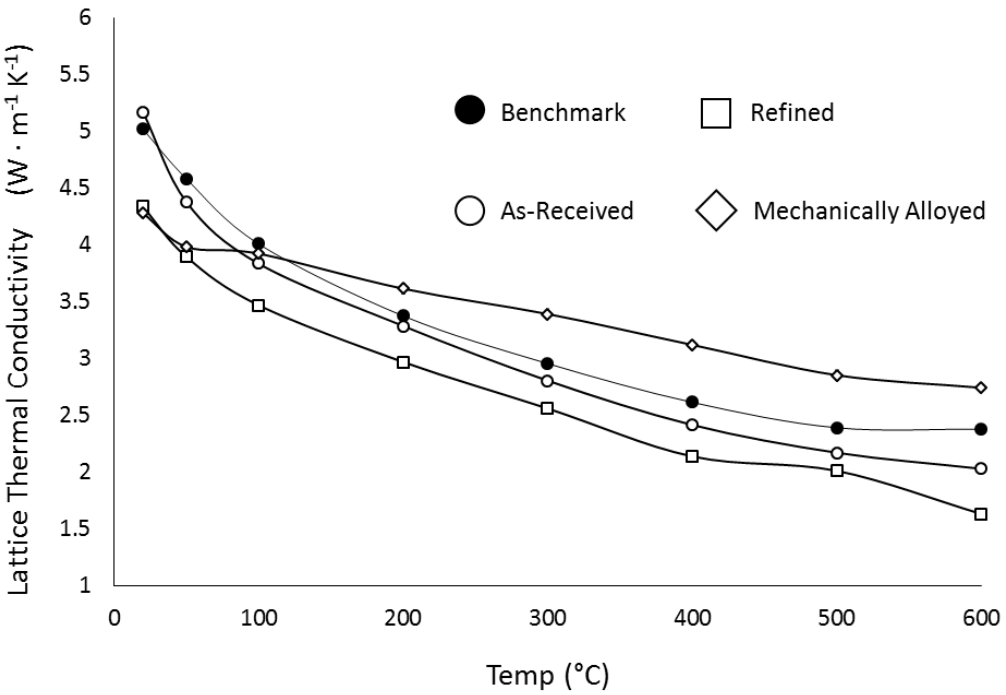

Figure 30: The lattice component of thermal conductivity for n-type half-Heusler compound with nominal composition of $Hf_{0.25}Zr_{0.75}NiSn_{0.99}Sb_{0.01}$. Solid lines are a guide for the eye.

Next, the highest performing p-type half-Heusler compound with nominal composition $Nb_{0.75}Ti_{0.25}FeSb$ is the benchmark material, with a peak ZT ≈ 0.9 at 600°C (Figure 31). This is despite the fact that all other materials sintered by SPS had a significantly higher power factor (Figure 32). The composition $Nb_{0.96}Ti_{0.04}FeSb$, which was expected to have the highest room-temperature power factor, does indeed have a power factor more than twice as high as the other materials. Unlike the ZrNiSn based compound, the NbFeSb based compound shows a strong dependence on the sintering temperature in SPS. This dependence is best illustrated by the power factor, which is much higher for materials sintered at 975°C (Figure 33). There is no evident dependence on dwell time, with materials being sintered at 925°C for either 5 or 10 minutes having

similar power factors. Only the materials sintered at 975°C for 10 minutes are considered in the other plots.

Although the Seebeck coefficient is nearly the same for the composition of $Nb_{0.75}Ti_{0.25}FeSb$ prepared by any method, that of the $Nb_{0.96}Ti_{0.04}FeSb$ composition reaches an exceptionally high value of more than 250 $\mu V \cdot K^{-1}$ at 600°C (Figure 34). However, a high figure of merit was not achieved by this composition because of its much lower electrical conductivity (Figure 35) due to a smaller charge carrier concentration. Although these materials have similar power factors to the n-type materials, they have significantly higher thermal conductivities (Figure 36) which limits their maximum ZT. Although the refining process greatly reduced the lattice thermal conductivity below the benchmark material for the n-type material, that was not the case for the p-type materials (Figure 37). It is possible that the benchmark material benefits, in terms of its thermal conductivity, from its multi-phase structure. Although the refining process greatly reduced grain size, the gains from nano-structuring may be offset by improving the phase-purity. The very high lattice thermal conductivity in the composition with much less Ti substitution highlights the benefits of alloy scattering. Although the highest performing material is the benchmark material, its properties are really the average of the multiple phases present in this material. The properties of the nearly single phase, mechanically alloyed composition of $Nb_{0.75}Ti_{0.25}FeSb$ are lower than the benchmark material with nominally the same composition. This suggests that 25% substitution of Ti for Nb is not necessarily the optimum doping level, and there is still room to improve this material.

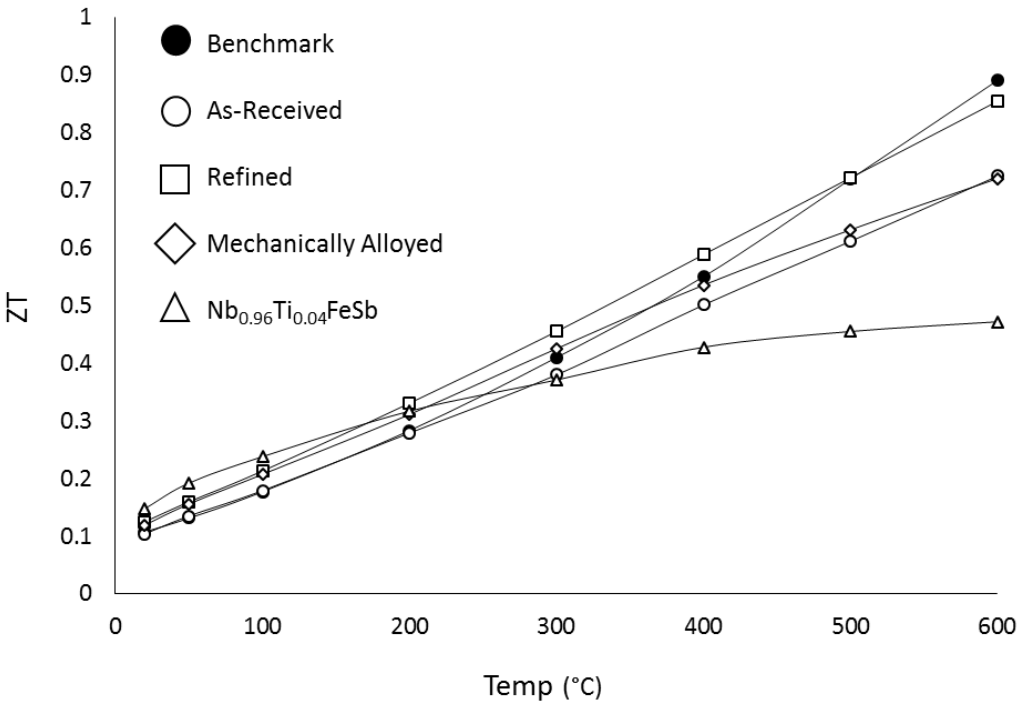

Figure 31: Thermoelectric figure of merit for p-type half-Heusler compounds with nominal compositions of $Nb_{0.75}Ti_{0.25}FeSb$ and $Nb_{0.96}Ti_{0.04}FeSb$. Solid lines are a guide for the eye.

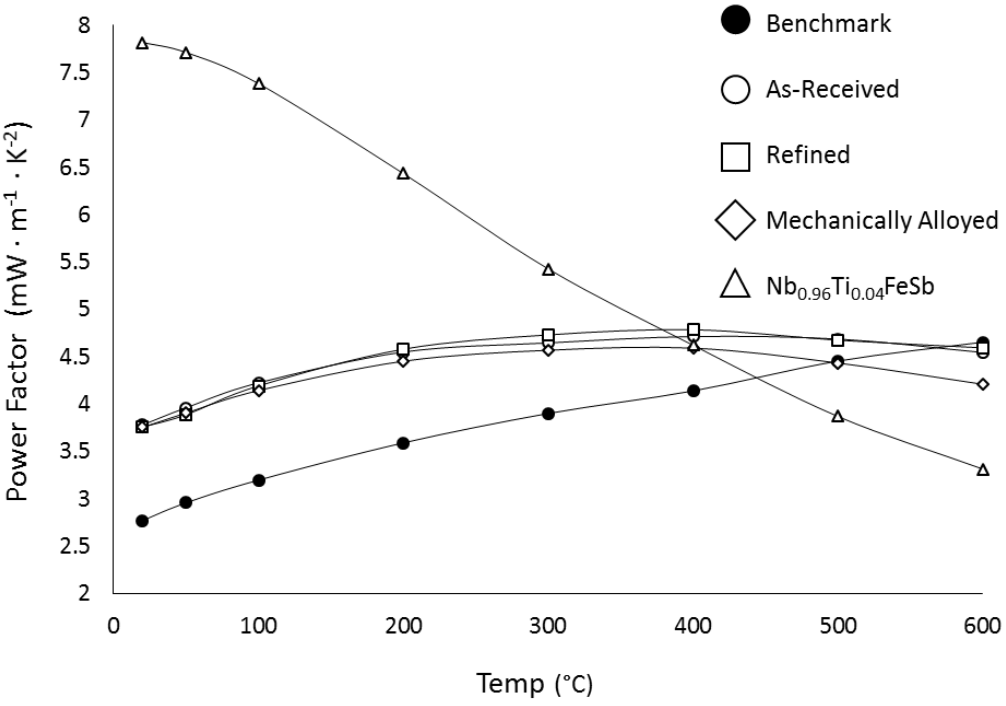

Figure 32: The calculated power factor for p-type half-Heusler compounds with nominal compositions of $Nb_{0.75}Ti_{0.25}FeSb$ and $Nb_{0.96}Ti_{0.04}FeSb$. Solid lines are a guide for the eye.

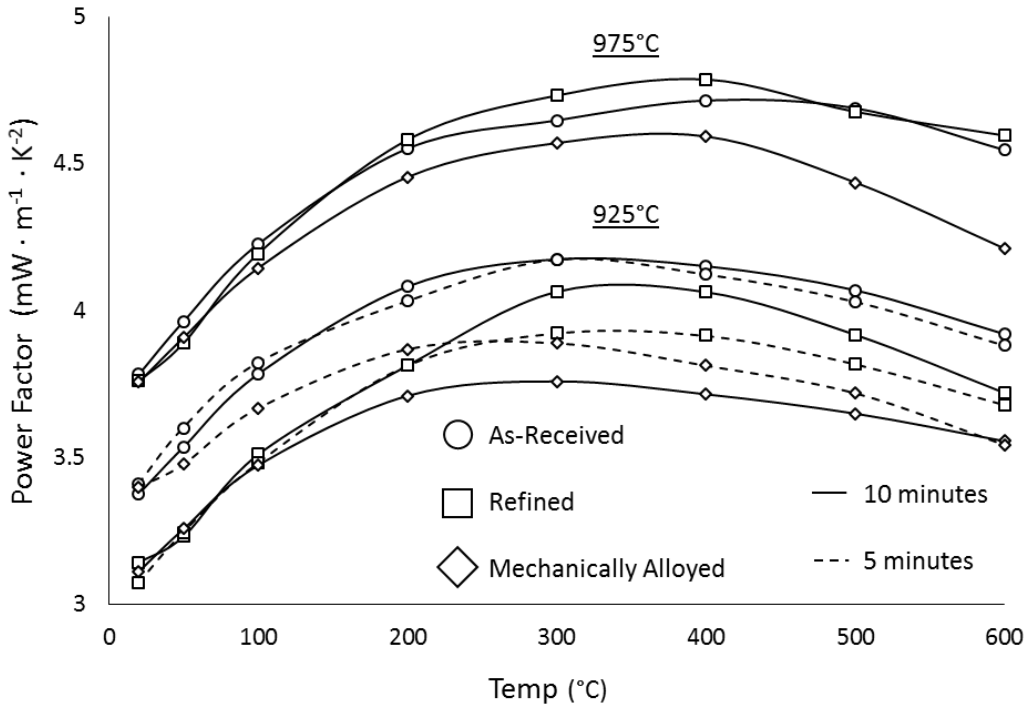

Figure 33: The calculated power factor for as-received, refined, and mechanically alloyed, p-type half-Heulser compounds with nominal compositions of $Nb_{0.75}Ti_{0.25}FeSb$ each sintered by SPS at either 925 or 975°C. Solid lines represent materials held at their maximum sintering temperature for 10 minutes, and dashed lines represent those held for 5 minutes. The power factor shows a strong dependence on sintering temperature, with those materials sintered at 975°C all having a much higher power factor.

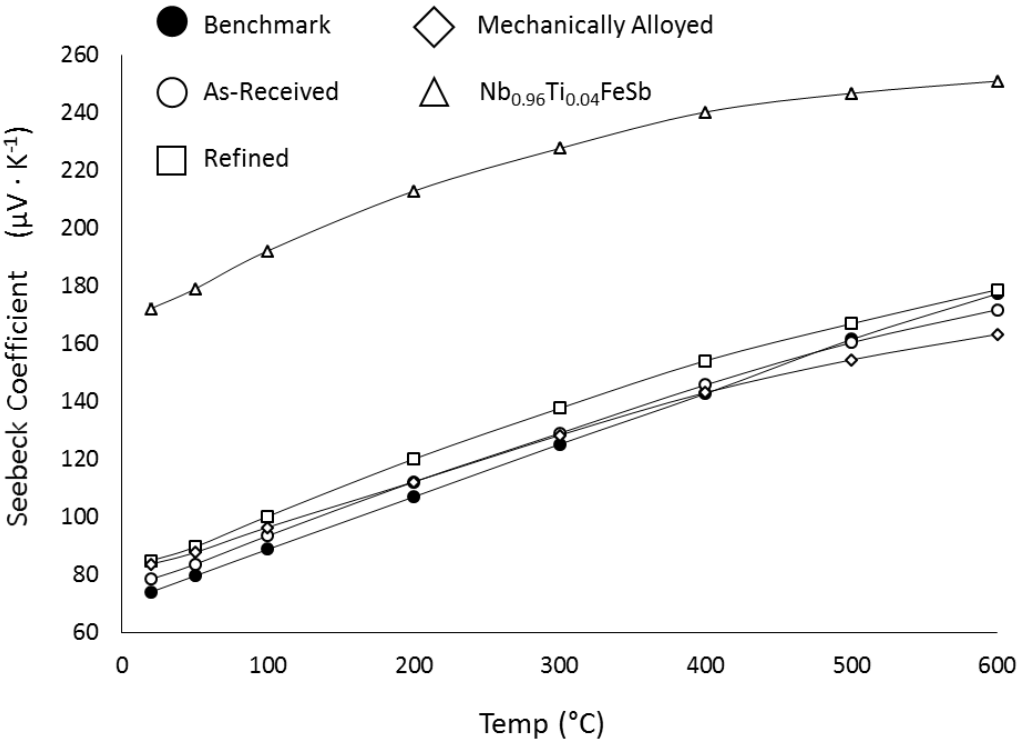

Figure 34: The Seebeck coefficient for p-type half-Heusler compounds with nominal compositions of $Nb_{0.75}Ti_{0.25}FeSb$ and $Nb_{0.96}Ti_{0.04}FeSb$. Solid lines are a guide for the eye.

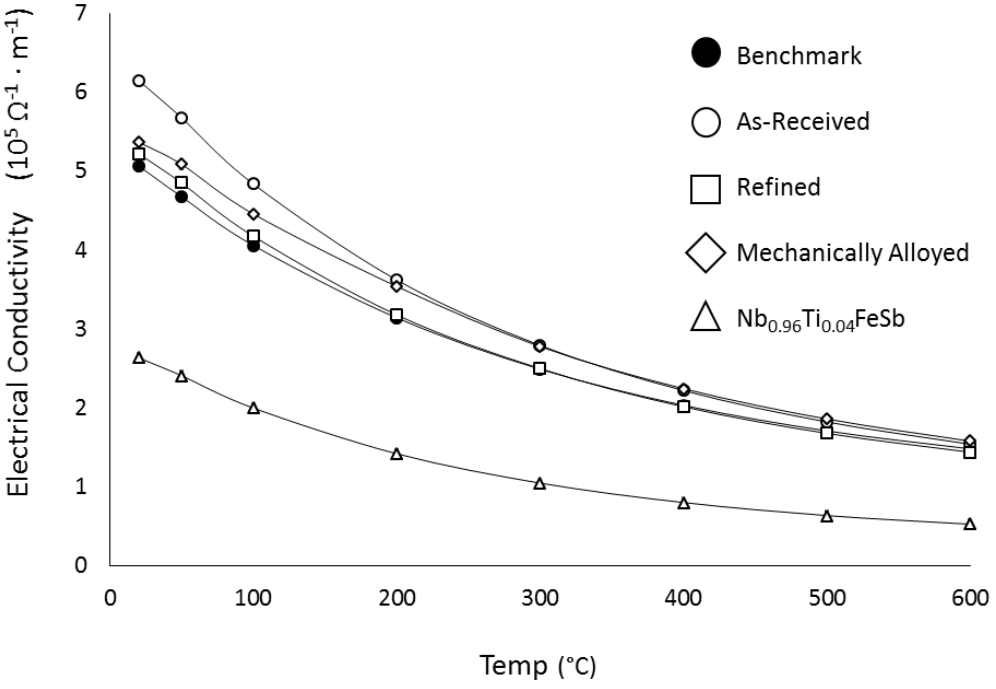

Figure 35: The electrical conductivity for p-type half-Heusler compounds with nominal compositions of $Nb_{0.75}Ti_{0.25}FeSb$ and $Nb_{0.96}Ti_{0.04}FeSb$. Solid lines are a guide for the eye.

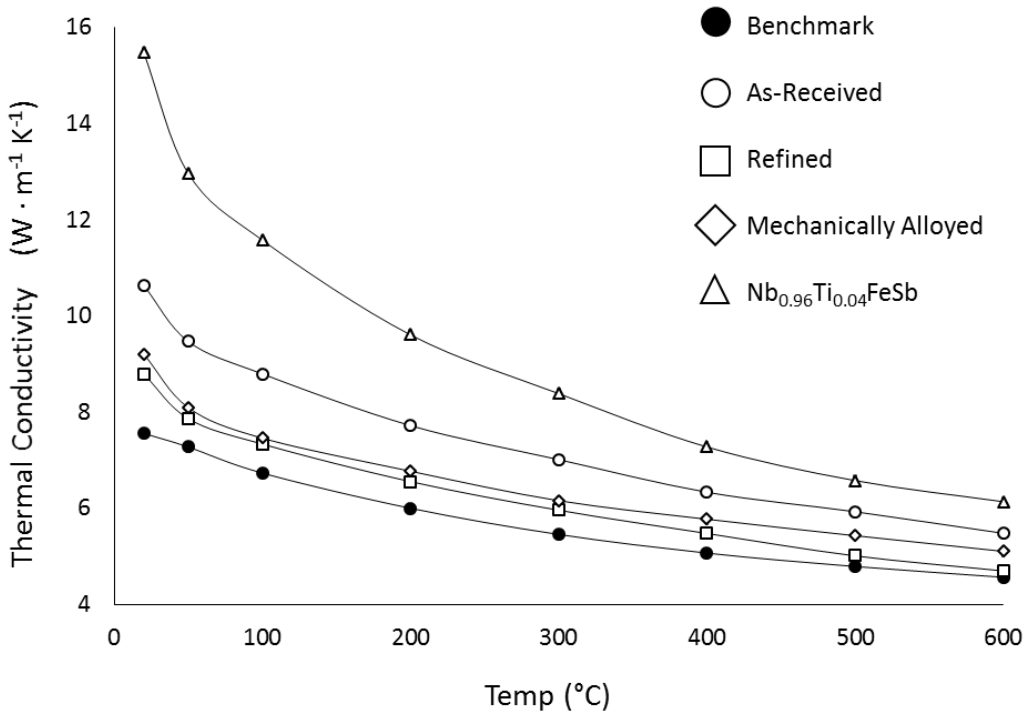

Figure 36: The total thermal conductivity for p-type half-Heusler compounds with nominal compositions of $Nb_{0.75}Ti_{0.25}FeSb$ and $Nb_{0.96}Ti_{0.04}FeSb$. Solid lines are a guide for the eye.

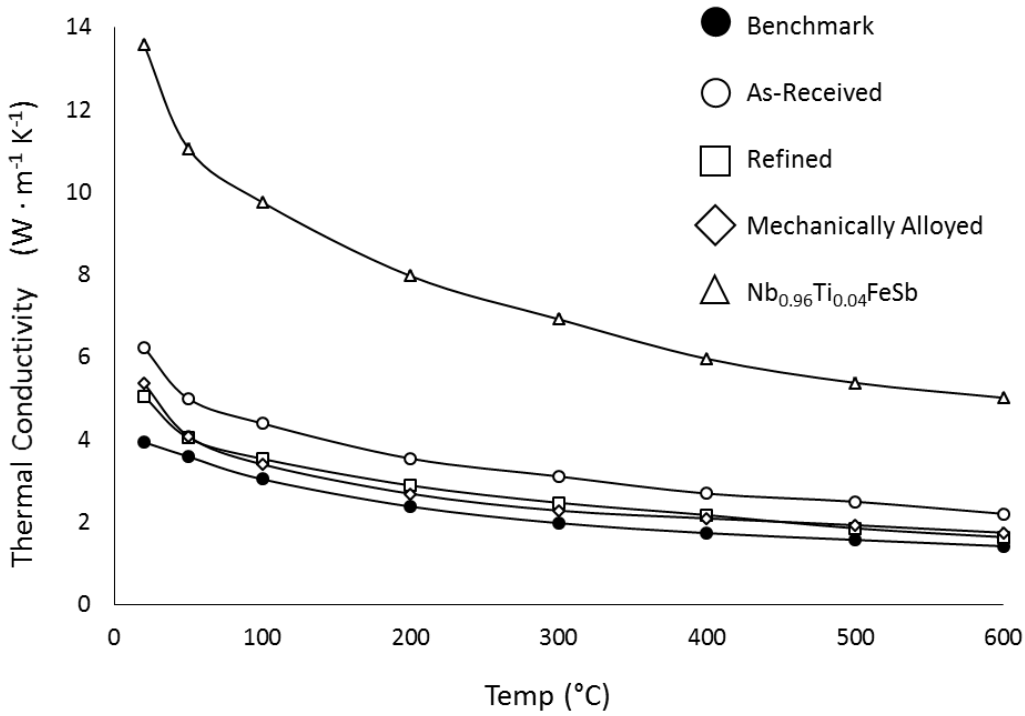

Figure 37: The lattice component of thermal conductivity for p-type half-Heusler compounds with nominal compositions of $Nb_{0.75}Ti_{0.25}FeSb$ and $Nb_{0.96}Ti_{0.04}FeSb$. Solid lines are a guide for the eye.

Finally, n- and p-type behavior are sought in the NbCoSn base composition by substituting Sn with the higher-valence element Sb and by substituting Nb with the lower valence element Ti. At the levels of 10 and 25% substitution of Ti for Nb, these materials showed essentially zero Seebeck coefficient and very low electrical conductivity at room-temperature. Above 300°C, these materials showed n-type behavior. This suggests that doping the NbCoSn composition with holes was only enough to suppress conduction from electrons but not enough to transition to extrinsic p-type behavior. The composition $Nb_{0.25}Ti_{0.75}CoSn$, which should have been heavily doped with holes, also shows n-type behavior and only moderate thermoelectric performance. For this reason, these compositions are not discussed any further.

However, the fully dense, nano-grained $NbCoSn_{0.9}Sb_{0.1}$ in the current study shows a similar, although slightly lower, power factor to the other material in the current work (Figure 38), and a 75% increase in ZT over the previously reported n-type materials of this composition, reaching a peak ZT ≈ 0.53 (Figure 39).[51,52] This is due to a 24% increase in the Seebeck coefficient (Figure 40), while at the same time retaining essentially the same electrical conductivity (Figure 41), and an 18% decrease in thermal conductivity at 600°C (Figure 42). The enhancement in Seebeck coefficient can be attributed to improving the phase purity. Despite having a higher density than previously reported, the ability of interfaces to suppress thermal conductivity by means of phonon scattering is again demonstrated in the present nano-grained material. This shows that there is still room to improve this half-Heusler composition by optimizing carrier concentration and lowering thermal conductivity by alloying.

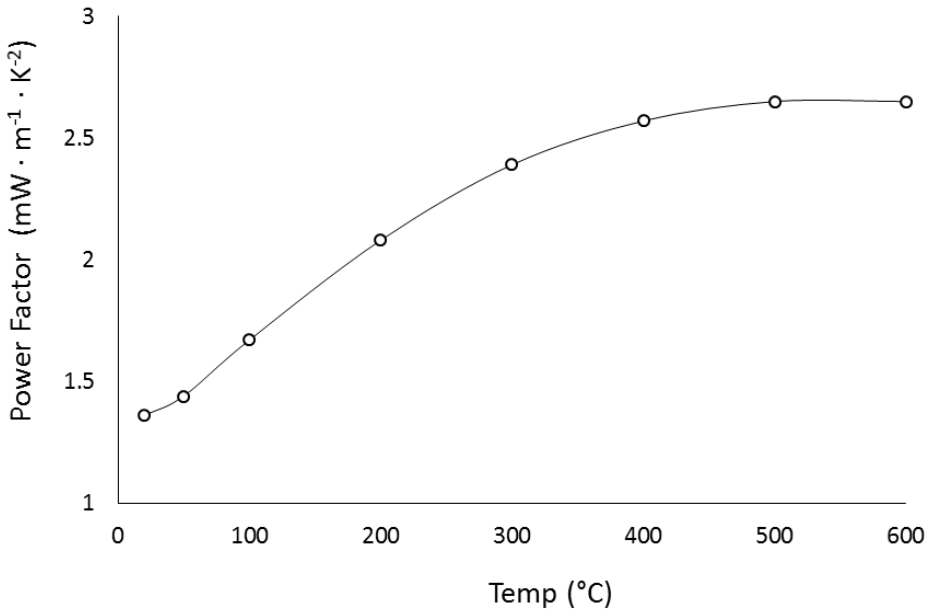

Figure 38: The calculated power factor for n-type half-Heusler compound with a nominal composition of $NbCoSn_{0.9}Sb_{0.1}$. The solid line is a guide for the eye.

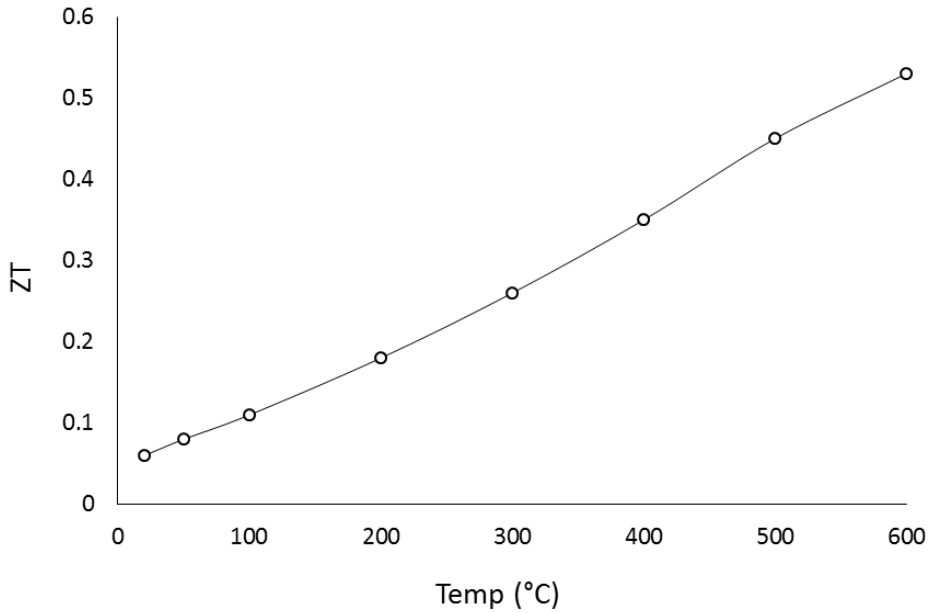

Figure 39: Thermoelectric figure of merit for n-type half-Heusler compound with a nominal composition of $NbCoSn_{0.9}Sb_{0.1}$. The solid line is a guide for the eye.

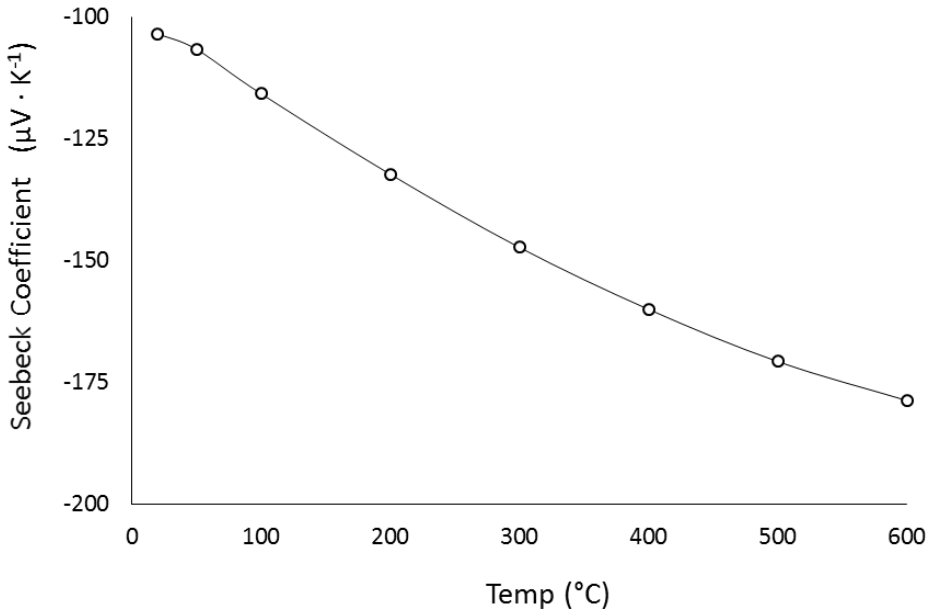

Figure 40: Seebeck coefficient for n-type half-Heusler compound with a nominal composition of $NbCoSn_{0.9}Sb_{0.1}$. The solid line is a guide for the eye.

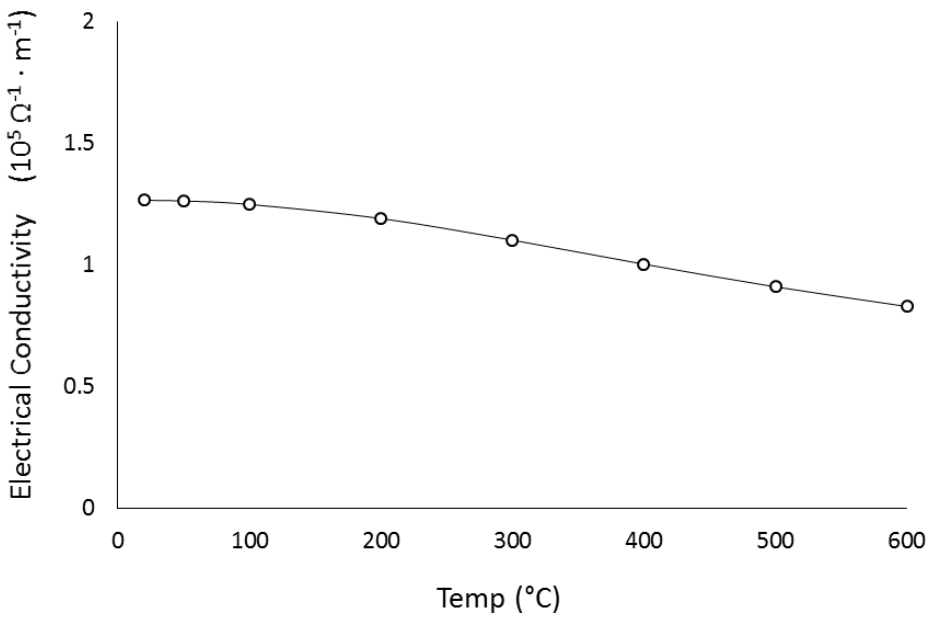

Figure 41: Electrical conductivity for n-type half-Heusler compound with a nominal composition of $NbCoSn_{0.9}Sb_{0.1}$. The solid line is a guide for the eye.

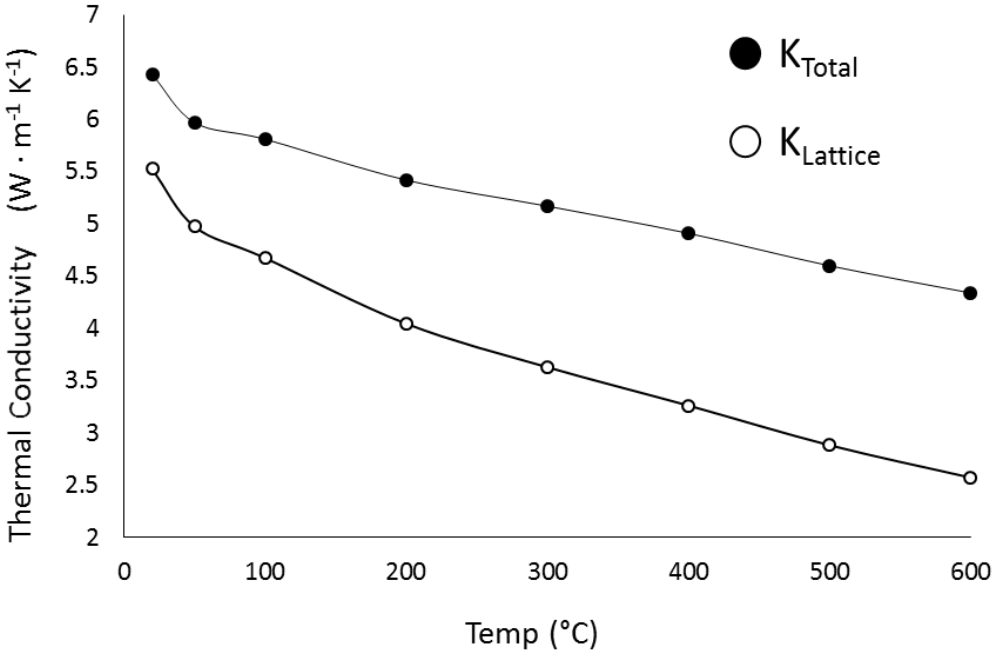

Figure 42: Thermal conductivity for n-type half-Heusler compound with a nominal composition of $NbCoSn_{0.9}Sb_{0.1}$. The total thermal conductivity is represented by closed circles and the lattice component of thermal conductivity is represented by open circles. Solids line are a guide for the eye.

CHAPTER FOUR: CONCLUSIONS AND FUTURE WORK

Thermoelectric half-Heusler compounds have potential to convert the heat wasted from industrial and transportation processes to useful electricity. In order for this to be a cost effect means of waste-heat recovery, the thermoelectric figure of merit, ZT, should exceed 2. Current state-of-the-art materials have peak ZT ≈ 1. Among the highest performing half-Heusler compounds are nano-structured bulk materials which have been arc-melted, pulverized into a nano-powder, and sintered by DC-hot press. High performing n- and p-type half-Heusler compounds with nominal composition of $Hf_{0.25}Zr_{0.75}NiSn_{0.99}Sb_{0.01}$ and $Nb_{0.75}Ti_{0.25}FeSb$, respectively, have been provided to us in both dense and powder form by our collaborators at the University of Houston. We consolidate these powders by SPS, refine these powders to improve both particle size and phase-purity, and synthesize these compositions by an alternative mechanical alloying process. In addition to these compositions, we investigate these same base compositions with different doping levels as well as compounds with different base compositions.

Characteristic of the benchmark material sintered by DC-hot press and the as-received powder sintered by SPS are grains ranging from sub-micrometer to larger than 20 μm. At least three distinct half-Heusler phases with compositions of $M_{1-x}M'_{x}Ni_{1+y}Sn$ are identified in these materials. Refining these powders by an additional milling process reduces the grain size to 660 ± 70 nm in materials sintered by SPS. This significantly lowered the lattice component of thermal conductivity in these materials. However, the

refined powders sintered by SPS had significantly lower Seebeck coefficients and higher electrical conductivities, which resulted in a lower power factor and higher thermal conductivity than the benchmark material. Ultimately, this lowered the overall performance to a peak ZT ≈ 0.9. This is likely due to the refining process alloying unmixed metal left over from the arc-melting process which increased the charge carrier concentration. The highest figure of merit was ZT ≈ 1.1 in the as-received material sintered by SPS.

Mechanical alloying was investigated in hopes to provide an alternative synthesis route to produce useful quantities of single-phase nano-powder while eliminating lengthy heat treatments and unnecessary processing steps which likely introduce impurities. This was not accomplished for (M)NiSn type compounds where (M = Hf, Zr, Ti) because the high room-temperature strength of Hf makes it difficult to mechanically alloy. However, the energy input can be increased in the high-energy planetary ball mill by increasing the rpm or by using larger media. Experiments are ongoing to successfully synthesize these compound by mechanical alloying.

Benchmark, p-type half-Heusler compounds with nominal composition of $Nb_{0.75}Ti_{0.25}FeSb$ were characterized by two distinct phases with very different compositions and a large quantity of impurity phases, such as Nb – Fe binary phases and unmixed Nb and Ti. As-received powders had a wide distribution of particle sizes ranging from sub-micron up to 100 μm and contained unmixed metals and binary phases. The refining process successfully eliminated these impurity phases and created a single half-Heusler composition, while at the same time reducing the particle size. Mechanical alloying was successful in producing single phase nano-powders in Hf-free, NbFeSb half-

Heusler compounds. Mechanically synthesized powders sintered by SPS had an average grain size of 440 ± 70 nm, however this did not reduce the lattice thermal conductivity below the benchmark material.

An exceptionally high, low-temperature power factor was demonstrated in a p-type compound with composition of $Nb_{0.96}Ti_{0.04}FeSb$. However, because of the low carrier concentration, this material had a low conductivity at high temperatures, and because of the low alloying level this composition had a very high thermal conductivity, and only reached a ZT ≈ 0.5. Although a high ZT ≈ 1 was achieved in the $Nb_{0.75}Ti_{0.25}FeSb$ composition, it is believed that this doping level is not optimal, and a systematic investigation in mechanically alloyed, $Nb_{1-x}Ti_xFeSb$ where ($0.04 \leq x \leq 0.25$), is ongoing.

Half-Heusler compounds with NbCoSn base composition, for the most part, have received very little attention. However, first-principle calculations have predicted that this composition could reach very high power factors in both the n- and p-type regimes. In the current work, p-type conduction was sought by substituting Nb with the lower valence element Ti. At the levels of 10 and 25% substitution of Ti for Nb, these materials showed essentially zero Seebeck coefficient and very low electrical conductivity. This suggests that doping the NbCoSn composition with holes was only enough to suppress conduction from electrons but not enough to transition to extrinsic p-type behavior.

However, mechanically synthesized $NbCoSn_{0.9}Sb_{0.1}$ in the current study shows a 75% increase in ZT over the previously reported n-type materials of this composition, reaching a peak ZT ≈ 0.53. This is due to a 24% increase in the Seebeck coefficient and an 18% decrease in thermal conductivity as a result of nano-structuring. There is ongoing

work to improve this half-Heusler composition by optimizing carrier concentration and lowering thermal conductivity, with possibilities to substitute for each Nb, Co, and Sn.

REFERENCES

1 U. S. Energy Information Administration. International Energy Outlook 2016. (2016).

2 The World Bank. High and Dry: Climate Change, Water, and the Economy. (2016).

3 Melillo, J. M., Richmond, T. T. & Yohe, G. Climate change impacts in the United States. *Third National Climate Assessment* (2014).

4 Fleurial, J.-P. Thermoelectric power generation materials: Technology and application opportunities. *Jom* **61**, 79-85 (2009).

5 Radousky, H. B. & Liang, H. Energy harvesting: an integrated view of materials, devices and applications. *Nanotechnology* **23**, 35, doi:10.1088/0957-4484/23/50/502001 (2012).

6 Bell, L. E. Cooling, heating, generating power, and recovering waste heat with thermoelectric systems. *Science* **321**, 1457-1461 (2008).

7 Vining, C. B. An inconvenient truth about thermoelectrics. *Nat. Mater.* **8**, 83-85 (2009).

8 Clayton, D. A., Andrews Jr, W. H. & Lenarduzzi, R. Power Harvesting Practices and Technology Gaps for Sensor Networks. *ORNL/TM-2012/442, Oak Ridge National Laboratory* (2012).

9 Kaldenbach, B. J. *et al.* Assessment of wireless technologies and their application at nuclear facilities. *U.S. NRC / ORNL* (2006).

10 Bos, J.-W. G. & Downie, R. A. Half-heusler thermoelectrics: A complex class of materials. *Journal of Physics: Condensed Matter* **26**, 433201 (2014).

11 Chen, S. & Ren, Z. Recent progress of half-Heusler for moderate temperature thermoelectric applications. *Mater. Today* **16**, 387-395 (2013).

12 Date, A., Date, A., Dixon, C. & Akbarzadeh, A. Progress of thermoelectric power generation systems: Prospect for small to medium scale power generation. *Renewable and Sustainable Energy Reviews* **33**, 371-381 (2014).

13 DiSalvo, F. J. Thermoelectric cooling and power generation. *Science* **285**, 703-706 (1999).

14 Zhao, J.-Y., Zhu, D.-S., Zhou, Z.-G., WANG, C.-h. & CHEN, H. Research progress of thermoelectric power generation [J]. *Chinese Journal of Power Sources* **3**, 031 (2010).

15 Minnich, A. J., Dresselhaus, M. S., Ren, Z. F. & Chen, G. Bulk nanostructured thermoelectric materials: current research and future prospects. *Energy Environ. Sci.* **2**, 466-479, doi:10.1039/b822664b (2009).

16 Xie, H. *et al.* Beneficial Contribution of Alloy Disorder to Electron and Phonon Transport in Half-Heusler Thermoelectric Materials. *Adv. Funct. Mater.* **23**, 5123-5130 (2013).

17 Biswas, K. *et al.* High-performance bulk thermoelectrics with all-scale hierarchical architectures. *Nature* **489**, 414-418 (2012).
18 Zhao, L.-D., Dravid, V. P. & Kanatzidis, M. G. The panoscopic approach to high performance thermoelectrics. *Energy Environ. Sci.* **7**, 251-268 (2014).
19 Sootsman, J. R., Chung, D. Y. & Kanatzidis, M. G. New and Old Concepts in Thermoelectric Materials. *Angew. Chem.-Int. Edit.* **48**, 8616-8639, doi:10.1002/anie.200900598 (2009).
20 Graf, T., Felser, C. & Parkin, S. S. Simple rules for the understanding of Heusler compounds. *Progress in solid state chemistry* **39**, 1-50 (2011).
21 Zeier, W. G. *et al.* Engineering half-Heusler thermoelectric materials using Zintl chemistry. *Nature Reviews Materials*, 16032 (2016).
22 Page, A., Poudeu, P. & Uher, C. A first principles approach to half-Heusler thermoelectrics: accelerated prediction and understanding of material properties. *Journal of Materiomics* (2016).
23 Yang, J. *et al.* Evaluation of Half-Heusler Compounds as Thermoelectric Materials Based on the Calculated Electrical Transport Properties. *Adv. Funct. Mater.* **18**, 2880-2888, doi:10.1002/adfm.200701369 (2008).
24 Chen, L. *et al.* Uncovering High Thermoelectric Figure of Merit in (Hf, Zr) NiSn Half-Heusler Alloys. *arXiv preprint arXiv:1505.07773* (2015).
25 Snyder, G. J. & Toberer, E. S. Complex thermoelectric materials. *Nat. Mater.* **7**, 105-114 (2008).
26 Li, J.-F., Liu, W.-S., Zhao, L.-D. & Zhou, M. High-performance nanostructured thermoelectric materials. *NPG Asia Materials* **2**, 152-158 (2010).
27 Liu, W., Yan, X., Chen, G. & Ren, Z. Recent advances in thermoelectric nanocomposites. *Nano Energy* **1**, 42-56 (2012).
28 Ren, Z. *et al.* (Google Patents, 2014).
29 Joshi, G. *et al.* Enhancement of thermoelectric figure-of-merit at low temperatures by titanium substitution for hafnium in n-type half-Heuslers Hf 0.75− x Ti x Zr 0.25 NiSn 0.99 Sb 0.01. *Nano Energy* **2**, 82-87 (2013).
30 Joshi, G. *et al.* Enhancement in Thermoelectric Figure-Of-Merit of an N-Type Half-Heusler Compound by the Nanocomposite Approach. *Advanced Energy Materials* **1**, 643-647 (2011).
31 Chen, L., Huang, X., Zhou, M., Shi, X. & Zhang, W. The high temperature thermoelectric performances of Zr0. 5Hf0. 5Ni0. 8Pd0. 2Sn0. 99Sb0. 01 alloy with nanophase inclusions. *Journal of applied physics* **99**, 064305 (2006).
32 Bhattacharya, S. *et al.* Effect of Sb doping on the thermoelectric properties of Ti-based half-Heusler compounds, TiNiSn1− xSbx. *Appl. Phys. Lett.* **77**, 2476-2478 (2000).
33 Szczech, J. R., Higgins, J. M. & Jin, S. Enhancement of the thermoelectric properties in nanoscale and nanostructured materials. *Journal of Materials Chemistry* **21**, 4037-4055 (2011).
34 Yan, X. A. *et al.* Enhanced Thermoelectric Figure of Merit of p-Type Half-Heuslers. *Nano Lett.* **11**, 556-560, doi:10.1021/nl104138t (2011).
35 Maji, P. *et al.* Thermoelectric performance of nanostructured p-type Zr 0.5 Hf 0.5 Co 0.4 Rh 0.6 Sb 1− x Sn x half-Heusler alloys. *Journal of Solid State Chemistry* **202**, 70-76 (2013).

36 Zou, M., Li, J.-F., Du, B., Liu, D. & Kita, T. Fabrication and thermoelectric properties of fine-grained TiNiSn compounds. *Journal of Solid State Chemistry* **182**, 3138-3142 (2009).

37 Yu, C. *et al.* High-performance half-Heusler thermoelectric materials Hf 1− x ZrxNiSn 1− ySby prepared by levitation melting and spark plasma sintering. *Acta Materialia* **57**, 2757-2764 (2009).

38 Xia, Y. *et al.* Thermoelectric properties of semimetallic (Zr, Hf) CoSb half-Heusler phases. *Journal of applied physics* **88**, 1952-1955 (2000).

39 Shutoh, N. & Sakurada, S. Thermoelectric properties of the Ti x (Zr 0.5 Hf 0.5) 1− x NiSn half-Heusler compounds. *Journal of alloys and compounds* **389**, 204-208 (2005).

40 Sakurada, S. & Shutoh, N. Effect of Ti substitution on the thermoelectric properties of (Zr, Hf) NiSn half-Heusler compounds. *Appl. Phys. Lett.* **86**, 082105 (2005).

41 Populoh, S. *et al.* High figure of merit in (Ti, Zr, Hf) NiSn half-Heusler alloys. *Scripta Materialia* **66**, 1073-1076 (2012).

42 Kurosaki, K., Muta, H. & Yamanaka, S. Thermoelectric properties of titanium-based half-Heusler compounds. *Journal of alloys and compounds* **384**, 51-56 (2004).

43 Kenjo, T., Kimura, Y. & Mishima, Y. in *MRS Proceedings.* 1218-Z1205-1214 (Cambridge Univ Press).

44 Joshi, G. *et al.* NbFeSb-based p-type half-Heuslers for power generation applications. *Energy Environ. Sci.* **7**, 4070-4076 (2014).

45 Zou, M., Li, J.-F., Guo, P. & Kita, T. Synthesis and thermoelectric properties of fine-grained FeVSb system half-Heusler compound polycrystals with high phase purity. *Journal of Physics D: Applied Physics* **43**, 415403 (2010).

46 Amornpitoksuk, P. & Suwanboon, S. Correlation of milling time on formation of TiCoSb phase by mechanical alloying. *Journal of Alloys and Compounds* **462**, 267-270 (2008).

47 Suryanarayana, C. Mechanical alloying and milling. *Progress in materials science* **46**, 1-184 (2001).

48 Ouardi, S. *et al.* Electronic transport properties of electron-and hole-doped semiconducting C 1 b Heusler compounds: NiTi 1− x M x Sn (M= Sc, V). *Physical Review B* **82**, 085108 (2010).

49 Fu, C. *et al.* Realizing high figure of merit in heavy-band p-type half-Heusler thermoelectric materials. *Nature communications* **6** (2015).

50 Wong-Ng, W. & Yang, J. International Centre for Diffraction Data and American Society for Metals database survey of thermoelectric half-Heusler material systems. *Powder Diffraction* **28**, 32-43 (2013).

51 Ono, Y., Inayama, S., Adachi, H. & Kajitani, T. in *Thermoelectrics, 2006. ICT'06. 25th International Conference on.* 124-127 (IEEE).

52 Kimura, Y., Tamura, Y. & Kita, T. Thermoelectric properties of directionally solidified half-Heusler compound NbCoSn alloys. *Appl. Phys. Lett.* **92**, 2105 (2008).

53 Downie, R., Barczak, S., Smith, R. & Bos, J. Compositions and thermoelectric properties of XNiSn (X= Ti, Zr, Hf) half-Heusler alloys. *Journal of Materials Chemistry C* **3**, 10534-10542 (2015).

54 Downie, R. A., Smith, R. I., MacLaren, D. A. & Bos, J.-W. G. Metal Distributions, Efficient n-Type Doping, and Evidence for in-Gap States in TiNiM y Sn (M= Co, Ni, Cu) half-Heusler Nanocomposites. *Chemistry of Materials* **27**, 2449-2459 (2015).

55 Melnyk, G., Leithe-Jasper, A., Rogl, P. & Skolozdra, R. The antimony-iron-niobium (Sb-Fe-Nb) system. *Journal of Phase Equilibria* **20**, 113-118, doi:10.1007/s11669-999-0009-x (1999).